Application of a coupled discontinuous–continuous Galerkin finite element shallow water model to coastal ocean dynamics

Cheryl Ann Blain *, T. Christopher Massey

Naval Research Laboratory, Oceanography Division, Ocean Dynamics and Prediction (Code 7322), Building 1009, C134, Stennis Space Center, MS 39529, USA

Abstract

A coupled discontinuous–continuous Galerkin (DG–CG) shallow water model is compared to a continuous Galerkin generalized wave-continuity equation (GWCE) based model for the coastal ocean, whereby local mass imbalance typical of GWCE-based solutions is eliminated using the coupled DG–CG approach. Two mass imbalance indicators for the GWCE-based model are presented and analyzed. The indicators motivate discussion on the suitability of using a GWCE-based model versus the locally conservative coupled DG–CG model. Both realistic and idealized test problems for tide, wind, and wave-driven circulation form the basis of the study. For the problems studied, coupled DG–CG solutions retain the robustness of well-documented solutions from GWCE-based models and also capture the dynamics driven by small-scale, highly advective processes which are problematic for GWCE-based models. Issues associated with the coupled DG–CG model are explored, including increased cost due to increased degrees of freedom, the necessary application of slope limiters, as well as the actual coupling process.
© 2004 Elsevier Ltd. All rights reserved.

Keywords: Shallow water equations; Discontinuous Galerkin methods; Coupled finite element methods; Generalized wave continuity equation; ADCIRC; Coastal ocean models; Mass error; Tidal dynamics; Rip currents; Bahamas, Bight of Abaco

---

* Corresponding author. Tel.: +1 228 688 5450; fax: +1 228 688 4759.
E-mail addresses: blain@nrlssc.navy.mil, cheryl.ann.blain@nrlssc.navy.mil (C.A. Blain).

1. Introduction

Since the construct of the wave-continuity equation (Lynch and Gray, 1979) two decades ago, finite element-based shallow water equation models have generated robust computations of tide and surge dynamics. These models typically utilize unstructured triangular grids which permit a large degree of flexibility in representing the complexities of the coastal ocean associated with convoluted shorelines and steep gradients in either currents or bathymetry and additionally accommodate the need for remote oceanic forcing. The recent availability of massively parallel computing resources has pushed the application of these models to higher and higher resolutions (down to meters) while capturing a more diverse array of smaller-scale physical processes present in the coastal ocean. One manifestation of these high resolution applications has been an increased occurrence of erroneous circulation fields whose errors can be attributed to the lack of enforcement in local mass conservation.

Mass imbalances in the transient solutions obtained from wave-continuity based finite element shallow water equation models were observed independently in 1992 by Kolar and Westerink (2000). A common source for these errors was determined to be the non-linear terms, particularly the advection terms. Since that time a number of efforts have been directed at removing or minimizing the presence of mass error in finite element-based computations. Improvements in the conservative properties of these models have come by applying a consistent treatment of the advective terms between the continuity and momentum equations as suggested by Kolar et al. (1994). A further reduction in mass error was realized by using mass conserving forms of the flux boundary conditions as proposed by both Lynch (1985) and Kolar et al. (1994). An entirely separate approach sought to mitigate mass conservation issues by constructing an "optimal" triangular mesh over which mass error is minimally uniform (Zhang and Baptista, 2000).

To date, mass errors still plague the solutions for some applications of finite element-based shallow water models that utilize the generalized wave continuity equation (GWCE) in place of the primitive form of the continuity equation. The GWCE (Kinnmark, 1986), a generalization of the wave-continuity equation formulation introduced by Lynch and Gray (1979), eliminates spurious oscillations that appeared in early finite element models that were based on the primitive continuity equation and used the same linear bases for both elevation and velocity. The absence of spurious spatial oscillations in the GWCE formulation is attributed to the monotonic dispersion relation that prevents the spurious, zero frequency, oscillations from forming while short wavelength modes ready propagate through the domain and do not accumulate energy (Walters, 1983). One consequence of using the GWCE has been the removal of the explicit enforcement of local (element by element) mass conservation.

While continuous Galerkin (CG) finite element-based shallow water equation models formally require global conservation (Lynch, 1985; Lynch and Holboke, 1997), the lack of local mass conservation remains problematic particularly for simulating small scale, highly advective flows and/or transport dynamics. One example is provided by Oliveira et al. (2000) who report the impact of flow mass errors on the fidelity of the computed mass transport for a tidally-driven application. For three-dimensional circulation problems, Luettich et al. (2002) demonstrate that significant errors in the vertical velocity result when mass errors are present in horizontal current fields. Thus, GWCE-based models have difficulty accurately capturing the vertical mixing and transport processes necessary to simulate flows dominated by density-driven dynamics. Of course, freshwater

river inflows and thermal mixing, processes that result from variations in the density field, can significantly contribute to the overall circulation of the coastal ocean. Though the past twenty years have seen very robust GWCE-based solutions for a large range of coastal flow problems (see the thorough review by Kolar and Westerink (2000)), as these models are pushed to represent small-scale, highly advective flows and transport processes, the GWCE formulation is becoming increasingly problematic. A new methodology is being sought that retains the advantages of unstructured triangular meshes but addresses the conservation issues associated with GWCE-based shallow water models.

A very new and promising class of finite element methods, the discontinuous Galerkin (DG) methods (Cockburn et al., 2000), have seen very rapid development over the last several years. The earliest applications of DG methods to the shallow water equations have taken the form of first order finite volume methods (Alcrudo and Garcia-Navarro, 1993; Chippada et al., 1998). Some applications to date have been limited to one dimension (Schwanenberg and Kongeter, 2000). Two-dimensional applications of the shallow water equations discretized using DG methods are limited in scope; many focus on the attributes of specific numerical schemes (e.g. Giraldo et al., 2002; Dawson and Proft, 2002) or provide only a cursory analysis of realistic applications (e.g., Schwanenberg and Kongeter, 2000; Aizinger and Dawson, 2002; Guillot and Blain, 2003).

The primary advantage of the discontinuous Galerkin methods with respect to mass conservation is their local (element by element) enforcement of the conservation laws. Other positive attributes are their ability to capture steep gradients and fronts, and a capability for using non-conforming unstructured meshes (i.e. elements of the mesh may have dissimilar interpolation points). The use of non-conforming grids simplifies the development of adaptive meshing strategies. The method has been shown to be second order accurate when applied over linear triangles (Dawson and Proft, 2002), an order of magnitude greater than finite volume methods and similar to current GWCE-based models. Furthermore, the local nature of the DG methods make them well suited for both h (mesh size) and p (approximation degree) adaptive schemes and are highly parallelizable.

This paper focuses on obtaining mass conserving, robust solutions to the shallow water equations by applying a coupled DG–CG (Dawson and Proft, 2002) shallow water equation model wherein the GWCE equation is entirely replaced by a DG primitive continuity equation, while the momentum equations are left untouched and solved with the usual continuous Galerkin formulation. For several representative coastal problems two non-dimensional quantities, R_{max}, the ratio of the mean maximum bathymetric difference to the element radius and, V, the time-integrated 2-D vorticity, are defined and evaluated for their suitability in predicting the spatial distribution and relative magnitudes of mass error in GWCE-based model solutions. A strong theoretical basis for these indicators links the mass error and local truncation error in GWCE-based models. A robust indicator of mass error is desirable to assess the need for a locally conservative computational algorithm, i.e. as that found within the coupled DG–CG model. Furthermore, such indicators could be used in the future to guide slope limiter application within DG methods or with so called flexible Galerkin algorithms for which some level of elemental continuity can be maintained (Massey, 2002). Following a demonstration of the viability of the two defined mass error indicators, the local mass error computed for the coupled DG–CG model is compared to the mass error associated with the GWCE-based model to confirm the conservative

nature of the coupled DG–CG method for a range of coastal ocean applications. Comparisons between the GWCE-based and coupled DG–CG solutions for two dynamically extreme coastal dynamics problems: (1) confirm that the new coupled DG–CG methodology retains the robustness of barotropic GWCE-based solutions for a typical non-linear tidal dynamics application and a fine-scale nearshore flow problem, and (2) demonstrates the influence of the conservative elevation solution of the coupled DG–CG implementation, and (3) provides evidence that the coupled DG–CG model may address limitations of the current GWCE-based finite element shallow water models for small-scale, highly advective flows as exemplified by a rip current nearshore circulation problem.

The paper proceeds as follows. Section 2 describes both the continuous Galerkin GWCE-based shallow water model and the coupled DG–CG formulation of the same model using the primitive continuity equation instead of the GWCE. Section 3 presents the methodology used for computing mass error and the evaluation of two indices for mass error. Section 4 presents comparisons of the mass error in GWCE-based solutions versus that computed for the coupled DG–CG model solutions as well as model-model comparisons of computed elevations and currents for two dynamically extreme coastal flow problems. Section 5 presents a discussion of issues associated with the use of slope limiting in a DG-based model and an analysis of the computational costs associated with the coupled DG–CG model. The paper ends in Section 6 with some concluding remarks about the use of the mass error indicators presented and the suitability of the coupled DG–CG model for application to coastal regions.

2. Shallow water models

A variety of coastal flow problems of considerable importance including tidal flows, storm surges, seiches, and pollutant dispersion can be described by the shallow water equations. Assuming density variations are small such that the fluid is incompressible and vertical accelerations of the fluid negligible, the shallow water equations can be derived by integrating the mass and momentum conservation laws over the water depth and assuming a hydrostatic pressure distribution. Note that for the formulation here the horizontal gradients of density are also neglected. The shallow water equations can then be written using the notation of Kolar et al. (1994). The primitive form of the conservation of mass equation is given by

$$L \equiv \frac{\partial \zeta}{\partial t} + \nabla \cdot (H\mathbf{v}) = 0, \tag{1}$$

and the conservative form of the momentum conservation equation is written:

$$\mathbf{M}^c \equiv \frac{\partial (H\mathbf{v})}{\partial t} + \nabla \cdot (H\mathbf{v}\mathbf{v}) + \tau H\mathbf{v} + H\mathbf{f} \times \mathbf{v} + \frac{H}{\rho}\nabla p_a + Hg\nabla(\zeta - \alpha\eta) - \mathbf{A} - \frac{1}{\rho}\nabla \cdot (H\mathbf{T}) = 0, \tag{2}$$

where ζ is the surface water elevation, H is the total water depth, $\mathbf{v}$ is the depth-averaged velocity vector, τ is the bottom friction coefficient, $\mathbf{f} = \mathbf{k}(2\Omega_E \sin\phi)$ is the Coriolis parameter with Ω_E as the angular velocity of the earth and ϕ degrees latitude, p_a is the atmospheric pressure, ρ is the density

of seawater, g is the gravitational acceleration, α is the effective Earth elasticity factor (0.69), η is the Newtonian equilibrium tide potential, $\mathbf{A}$ is the surface stress vector, and $\mathbf{T}$ is the Reynolds stress tensor. For this paper, the shallow water Eqs. (1) and (2) serve as the point of departure for the presented analyses.

2.1. A continuous Galerkin finite element model, ADCIRC

One widely-used continuous Galerkin finite element model is ADCIRC (the ADvanced CIR-Culation model for Shelves, Coasts and Estuaries, developed by Luettich and Westerink (Luettich et al., 1992; Luettich and Westerink, 2003). A successful history of accurate ADCIRC model simulations for tides (Westerink et al., 1994; Fortunato et al., 1998; Luettich et al., 1999) and storm surge (Blain et al., 1994, 1998) is well-documented. Most recently ADCIRC has been shown to reasonably capture the primary features associated with wave-driven flows such as alongshore currents (Blain and Cobb, 2003) and rip currents (Cobb and Blain, 2003).

Reviews by Navon (1988) and Westerink and Gray (1991) and more recently the discussion by LeRoux et al. (1998) highlight issues associated with solving the shallow water Eqs. (1) and (2) using finite element methods. These issues stem from the presence of spurious modes in solutions obtained using linear basis functions for both elevation and velocity within the primitive form of the continuity Eq. (1). As mentioned in the introduction, the use of a generalized wave continuity equation is one approach developed to eliminate this problem. The generalized wave continuity equation (GWCE) is expressed as

$$W^G \equiv \frac{\partial L}{\partial t} + GL - \nabla \cdot (\mathbf{M}^c) = 0, \tag{3}$$

where G is a numerical parameter that determines the balance between the primitive and wave forms of the continuity equation, e.g. for $G \to \infty, W^G \to L$. The pure wave continuity equation as presented by Lynch and Gray (1979) is obtained for $G = \tau$. The substitution of Eqs. (1) and (2) into Eq. (3) results in the GWCE:

$$W^G \equiv \frac{\partial^2 \zeta}{\partial t^2} + G\frac{\partial \zeta}{\partial t} + (G - \tau)\nabla \cdot (H\mathbf{v}) + \nabla$$
$$\cdot \left\{ \nabla \cdot (H\mathbf{vv}) + H\mathbf{f} \times \mathbf{v} + \frac{H}{\rho}\nabla p_a + Hg\nabla(\zeta - \alpha\eta) - \mathbf{A} - \frac{1}{\rho}\nabla \cdot (H\mathbf{T}) \right\} - H\mathbf{v} \cdot \nabla\tau = 0. \tag{4}$$

Furthermore, a non-conservative form of the momentum equation can be defined as,

$$\mathbf{M}^{nc} \equiv \frac{1}{H}(\mathbf{M}^c - \mathbf{v}L) = 0. \tag{5a}$$

After substituting Eqs. (1) and (2) into Eq. (5a), the non-conservative momentum equation reads:

$$\mathbf{M}^{nc} \equiv \frac{\partial \mathbf{v}}{\partial t} + \mathbf{v} \cdot \nabla\mathbf{v} + \tau\mathbf{v} + \mathbf{f} \times \mathbf{v} + \frac{1}{\rho}\nabla p_a + g\nabla(\zeta - \alpha\eta) - \frac{\mathbf{A}}{H} - \frac{1}{\rho H}\nabla \cdot (H\mathbf{T}) = 0. \tag{5b}$$

The ADCIRC model solves the generalized wave continuity Eq. (4) and the non-conservative momentum Eq. (5b). The advective terms in the GWCE (4) are reformulated to be consistent with the advection terms in Eq. (5b) (see Kolar et al., 1994 for specific details). The ADCIRC model is discretized using continuous Galerkin finite elements. The method of weighted residuals is applied to discretize Eqs. (4) and (5b). For this approach the approximate solution to Eqs. (4) and (5b), written in terms of basis functions, is substituted into the discrete equations. These equations are then multiplied by a weighting function and integrated over the entire domain. The objective is to generate a set of algebraic equations that allow for the solution of the unknowns introduced by the approximate solution through a minimization of the residual. The error between the approximate and exact solution is projected (or made zero) with respect to the weighting functions. The domain is divided into subdomains defined by triangular elements. The integrals then can be recast as a summation over the discrete elements.

For the Galerkin method the basis and weighting functions are identical and for the ADCIRC model are defined for linear triangles. The linear basis functions have a value of unity at one vertex of the triangle (identified as a node) and zero at the remaining two vertices of each triangle. For the continuous method, each basis function is selected to have C^0 (functional) continuity at the nodes. Thus the basis function defined at a given node has support over all of the triangular elements that share that node. This definition of the basis functions is an important distinction between the GWCE model and the coupled DG–CG that is to be described subsequently.

To reduce the order of the derivatives within the integrals of the residual, integration by parts is undertaken. The result is two integral terms, one of which is a boundary integral where the boundary is defined to enclose the entire domain; the boundary integral terms at shared element interfaces identically cancel for the continuous Galerkin method leaving only the boundary integral around the domain as a whole.

The semi-implicit time discretization of the GWCE uses a three-time-level approximation in which non-linear terms are treated explicitly while the time discretization of the momentum equation uses a lumped, two-time-level approximation. In a similar way to the GWCE, the non-linear terms within the momentum equation are linearized by formulating non-linear terms explicitly. From these time discretized equations, a time splitting procedure has been adopted wherein the GWCE is first solved for sea surface elevation and the momentum equation is then solved for the depth-averaged velocities.

2.2. A coupled continuous–discontinuous Galerkin finite element model

DG methods which are locally conservative by their definition were first introduced in the early 1970's by Reed and Hill (1973) for the transport of neutrons. The DG method applied here can be seen as a higher-order generalization of the popular finite volume (FV) methods and offers even more accuracy and flexibility than FV methods. Very recent advancements in higher-order DG methods, for example the so called Runge–Kutta discontinuous Galerkin (RKDG) method of Cockburn et al. (1990) and Cockburn and Shu (1998), have resulted in both accurate and convergent properties of the computed solution. Their RKDG method consists of three main parts: (i) a DG discretization in space with polynomials of order p, (ii) an explicit total variation bounded, TVB, Runge–Kutta time stepping scheme of order $p + 1$, and (iii) a generalized slope limiter to minimize overshoots and undershoots.

The coupled DG–CG model applied is a modified version of ADCIRC in which the GWCE formulation for elevation, Eq. (4), has been replaced with a RKDG formulation of the continuity equation in primitive form (1), while the solution of the momentum Eq. (5b) is left unchanged. This new version of the code, referred to as DG-ADCIRC, was written by Clint Dawson who has documented the methodology in Dawson et al. (2004). For completeness, a brief summary of this method is included here in Fig. 1.

Development of the DG discrete form of the primitive mass continuity Eq. (1) follows the same method of weighted residual procedure as outlined for the continuous Galerkin model. A primary difference lies in the definition of the basis functions. Linear basis functions are defined over a single element only; the basis functions for each element are in the polynomial space $\mathcal{V}^1 = \{1, x - x_e, y - y_e\}$, where (x_e, y_e) is the coordinate of the barycenter of the element. Thus the DG solution for elevation on each element is a linear two dimensional function expressed as,

$$\zeta(x, y, t)|_{\Delta_e} = c_{1,e}(t) + c_{2,e}(t)(x - x_e) + c_{3,e}(t)(y - y_e). \tag{6}$$

The basis functions and the elevation solution between adjacent elements have no continuity restraints imposed. Following integration by parts of the weighted residual statement, the integral terms that remain include boundary integral terms at every element edge. These terms do not cancel one another since no solution continuity between elements is imposed. The result is a flux term, $F(\mathbf{v}, \zeta_+^e, \zeta_-^e) \cdot \mathbf{n}_e$, containing the unique solution of the DG equation from the left, ζ_-^e, and right, ζ_+^e,
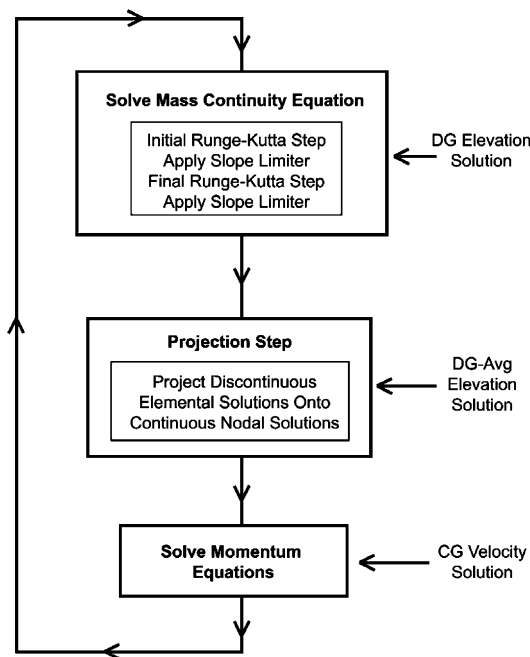

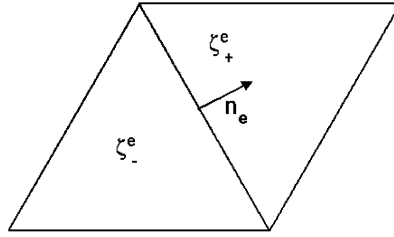Fig. 1. A simplified flowchart for the coupled DG–CG model.

Fig. 2. Two elements, along with the values of ζ_e to the left and right of the common edge, determined by the normal vector n_e.

side of a shared element edge, see Fig. 2. This flux term is numerically approximated using a Roe flux (see Dawson et al., 2004) which incorporates upwinding. Although the solution is discontinuous across an edge, the flux is unique and hence continuous. The resulting discrete DG form of the primitive continuity equation is given for $t > 0$ as

$$\int_{\Omega_e} \frac{\partial \zeta^e}{\partial t} w_e \, d\Omega_e - \int_{\Omega_e} \mathbf{v} H \nabla w_e \, d\Omega_e + \int_{\partial \Omega_e} F(\mathbf{v}, \zeta_+^e, \zeta_-^e) \cdot \mathbf{n}_e w_e d(\partial \Omega_e) = 0, \quad \forall w_e \in \mathscr{V}^1. \tag{7}$$

An explicit second order Runge–Kutta scheme for the time discretization of the discrete form of Eq. (1) yields a RKDG formulation for Eq. (7) that is solved element by element at each time step. After each intermediate time step of the Runge–Kutta scheme a conservative slope limiter is applied. Slope limiters are used in the RKDG and indeed most DG methods in order to ensure stability of the solution. The main function of the slope limiter is to minimize so called overshoots and undershoots of solutions, i.e. to control spurious oscillations. For non-linear problems and higher order methods, the use of slope limiters is a virtual must. A variety of slope limiters can be employed, yet to ensure the method stays locally conservative, one criterion of slope limiters that must be enforced is that the action of the slope limiter leave the average value of the solution over an element unchanged. The coupled DG–CG model currently uses a very simple yet conservative limiter based on a linear reconstruction scheme, the details of the slope limiter are provided in Appendix A.2. For the sake of convenience, in the remainder of this work whenever we refer to a DG method, it is to be understood that we mean a Runge–Kutta discontinuous Galerkin method, RKDG.

In order to solve the continuous Galerkin formulation of the momentum equation as originally formulated in ADCIRC, a continuous elevation solution must be passed to the momentum equation. To accomplish this, the elevation at a node is solved for by considering the DG elevations, defined over a single element, at all elements connected to a given node. The procedure basically leads to a L_2 weighted averaging of the DG solution back onto the nodes. The notation DG-Avg is used to indicate the continuous elevation and velocity solutions produced by the coupled DG–CG model. To be consistent with the ADCIRC formulation, mass lumping is used while determining the mass accumulation term. Furthermore on elevation specified boundary nodes, the specified elevation is enforced through the boundary flux term, a weak condition. The continuous nodal values for elevation, DG-Avg, are then used to solve the momentum Eq. (3) at the current time step in the same manner as described in Section 2.1. The nodal averaging could be eliminated

by changing the momentum equation implementation in ADCIRC, via integration by parts, so that either an element averaged elevation or edge flux, both of which are readily available, would be required. This is the subject of a possible future change to the implementation of the DG–CG formulation in ADCIRC.

Though a rigorous analysis of $2\Delta x$ wave formation and propagation within coupled DG–CG model solutions is not undertaken here, Cockburn and Shu (1998) have shown under certain grid requirements and through the use of appropriate slope limiters that the RKDG method when applied to hyperbolic conservation laws, like Eq. (1), is a stable, convergent method and thereby controls spurious oscillations. The wave propagation characteristics and convergence properties of a GWCE and a coupled DG–CG shallow water model are compared in Dawson et al. (2004). They apply both models to the weakly non-linear quarter annular harbor test case (Lynch and Officer, 1985) that has been accepted and used historically as a rigorous benchmark of model accuracy. Dawson et al. (2004) find small node-to-node oscillations in the direction of wave propagation for both the GWCE and the coupled DG–CG model solutions with oscillations for the coupled DG–CG model being slightly larger as expected. However, the second order accuracy and stability of the coupled DG–CG is retained through appropriate application of slope limiters (Dawson and Proft, 2002). Furthermore, the localized nature of the method means that node-to-node oscillations remain local to the individual element and do not propagate throughout the domain.

3. Characterization of the mass error in GWCE-based models

For the analyses contained herein, mass error is computed locally using an integral form of the mass conservation law shown by Eq. (1):

$$\int_{t_0}^{t} \int_{\Omega_e} \left[\frac{\partial \zeta}{\partial t} + \nabla \cdot (H\mathbf{v}) \right] \mathrm{d}\Omega_e \, \mathrm{d}t = 0, \tag{8}$$

where Ω_e is an element. Time integration of the first term of Eq. (8) and an application of the divergence theorem to the second term in Eq. (8) gives:

$$\int_{\Omega_e} (\zeta_t - \zeta_{t_0}) \, \mathrm{d}\Omega_e + \int_{t_0}^{t} \left[\int_{\partial\Omega_e} H\mathbf{v} \cdot \mathbf{n}_e \, \mathrm{d}(\partial\Omega_e) \right] \mathrm{d}t = 0. \tag{9}$$

A discrete form of Eq. (9) is obtained by approximating the dependent variables by their discrete counterparts following the procedure outlined by Kolar et al. (1994). The first term of Eq. (9) is evaluated exactly and expressed:

$$\int_{\Omega_e} (\zeta_t - \zeta_{t_0}) \, \mathrm{d}\Omega_e = (\zeta_t^e - \zeta_{t_0}^e) A_e, \tag{10}$$

where A_e is the area of element Ω_e and ζ_t^e is the elemental value of ζ_t^e. The boundary integral in Eq. (9) represents the net flux into the element when $\mathbf{n}_e$ is taken as the unit outward normal. For the second term in Eq. (9), expansion of H and $\mathbf{v}$ in terms of their basis functions (linear triangles) leads to an exact expression for the net flux, Q_{net}:

$$Q_{\text{net}} \equiv \int_{\partial\Omega_e} H\mathbf{v} \cdot \mathbf{n}_e d(\partial\Omega_e) = \sum_{e_b} \frac{L_e}{6} [2H_1 v_{n1} + H_1 v_{n2} + H_2 v_{n1} + 2H_2 v_{n2}], \tag{11}$$

where L_e is the length of an edge of the element Ω_e, $v_n = \mathbf{v} \cdot \mathbf{n}_e$, the sum is over all edges of the element and subscripts 1 and 2 refer to the nodes (numbered locally) at the end of the element edge. The time integral of Q_{net} from Eq. (9) is approximated using the trapezoid rule. The result,

$$E_{\text{mass}} = \left(\zeta_t^e - \zeta_{t_0}^e\right)A_e + \sum_k \frac{1}{2}\left[Q_t^{\text{net}} + Q_{t+\Delta t}^{\text{net}}\right]\Delta t, \tag{12}$$

is a discrete expression for the elemental mass error, E_{mass}. The first term represents the accumulation of mass over the element, Ω_e, from initial time, t_0, to a time, t. The second term in Eq. (12) is the net flux of mass into the element over the time interval $[t_k, t_k + \Delta t]$, summed over all time increments, k, contained in the time interval $[t_0, t]$. For perfect mass conservation, E_{mass} is equal to zero. A normalized elemental mass error is obtained by dividing the elemental mass error by the elemental volume,

$$E_{\text{mv}} = \frac{E_{\text{mass}}}{\text{Vol}_e}, \tag{13}$$

where Vol_e is the discrete volume of the water column defined by element, Ω_e, integrated approximately in time over each time interval $[t_k, t_k + \Delta t]$ via the trapezoid rule, then summed over all time increments, k, contained in the time interval $[t_0, t]$. Throughout the remainder of the text the mass error, E_{mass}, is computed as a dimensionless quantity, E_{mv} and reported as mass error in dimensionless units. More insight into the generation of mass error is provided using this technique over a simple examination of the global boundary fluxes, e.g. Aizinger and Dawson (2002).

Some may argue that the discrete mass flux should be computed in a way that is consistent with the finite element discretization within the numerical model (e.g. Berger and Howington, 2001). For a GWCE-based shallow water model, a consistent discrete numerical flux does not correspond to the physical flux (Massey and Blain, 2004) so that meaningful interpretation of the numerical flux is not readily apparent. Alternatively, the approach adopted here for computing mass error is consistent not only with a physical interpretation of Eq. (1) but also with the flux quantities that are relevant to transport processes.

3.1. Indicators of mass error

Proper representation of the circulation dynamics requires enough grid points to resolve sharp changes in the bathymetric gradient as demonstrated by Luettich and Westerink (1995) and Hagen et al. (2001). However it is not sufficient to remove all errors in the computed fields, i.e. (Hannah and Wright, 1995). This residual error may be attributed to mass imbalance. The location of maximum local mass error commonly is thought to be coincident with steep bathymetric gradients and/or complex coastal geometry. This characterization of local mass error is incomplete since these features are prevalent throughout most coastal and estuarine waters and robust solutions for a range of barotropic dynamics in these situations are known to be produced by GWCE-based models. Furthermore, Oliveira et al. (2000) note the correlations between bottom slopes and elemental mass error proved inconclusive in their estuarine application.

In order to better predict the occurrence of mass error in computed solutions, two quantities are defined here that parameterize either the local geometry considering both bathymetry and grid resolution or the dynamics of the flow field as represented by velocity gradients in the form of vorticity. The first non-dimensional quantity, R_{max}, is defined at each element as a ratio of the mean maximum bathymetric difference to the element radius. The mean maximum bathymetric difference is determined by first finding the maximum change in bathymetry between an element node and its neighbor nodes, then averaging those maximum changes to obtain a mean maximum bathymetric difference for the element. The element radius is defined to be the radius of the circle that circumscribes the element and is denoted by Δx_e. The combination of large bathymetry changes and/or fine mesh resolution yields the largest values of R_{max}. The R_{max} tracks not only bathymetric gradients but also the steepness of the gradient in relation to its resolution, particularly for uniform meshes. Note that R_{max} is a static value dependent only upon the computational mesh and the bathymetry and does not account for the dynamical solution in any way. As a result, extreme R_{max} values will identify regions in the mesh where local mass imbalance is likely to occur consistently, irrespective of the flow dynamics. Such a measure is convenient in that no computed solution is required to assess mass error given a mesh, its associated resolution and bathymetry gradients.

The second non-dimensional quantity defined, V, is simply the two-dimensional vorticity of the flow integrated in time over the interval $[t_k, t_k + \Delta t]$ via the trapezoid rule, and summed over all time increments, k, contained in the time interval $[t_0, t]$,

$$V = \left[\left(\frac{\partial v}{\partial x} - \frac{\partial u}{\partial y} \right)_{t_k} + \left(\frac{\partial v}{\partial x} - \frac{\partial u}{\partial y} \right)_{t_k + \Delta t} \right] \frac{\Delta t}{2}, \tag{14}$$

where u and v are the horizontal velocity components in the x and y coordinate directions. The time integration is performed to non-dimensionalize the quantity, V, and is consistent with the time integration involved in the computation of local mass imbalance, E_{mv}. The vorticity provides a visual indicator for the significance of velocity shear and advection since intuitively one's eye is drawn to regions showing extreme changes in the vorticity (i.e. vorticity gradients). As one example for wave-driven flows, high vorticity is an indicator of wave-breaking which is associated with strong velocity shear Buhler and Jacobson (2001) and is a common feature associated with near-shore dynamics. The discrete vorticity is well defined on each element and is easily computed from the readily available velocity solution, even after a relatively short duration simulation. The selection of vorticity as an indicator for mass error derives its theoretical basis from the analysis of Hagen et al. (2000). In their analyses the leading term of the local truncation error for the momentum equations in the GWCE-based model over structured grids is determined to be second order with respect to velocity and elevation gradients (see Appendix A.3 for the full expression of the local truncation error, LTEA, Eq. (A.3.1)). If one computes the gradient of the vorticity in Eq. (14) assuming uniform grid spacing, the four velocity gradient terms that arise are nearly identical to those expressed in the first term of the LTEA (LTEA$_1$, Eq. (A.3.2)). Therefore, the spatial derivatives of vorticity are expected to yield a similar pattern of error as the leading truncation error term of Hagen et al. (2000). In our analysis of vorticity as a visual indicator of mass error we will demonstrate a positive relationship between mass error, the LTEA and LTEA$_1$, and the

vorticity gradients. In order to proceed, a vorticity gradient represented as a discrete dimensionless term on each element Ω_e, is defined as,

$$\|D(V)_e\| \doteq \left\| \sum_k \int_{t_k}^{t_k+\Delta t} \nabla \left(\frac{\partial v}{\partial x} - \frac{\partial u}{\partial y} \right) \mathrm{d}t \right\| \Delta x_e, \tag{15}$$

where $\| \cdot \|$ is the regular Euclidean norm of the time-integrated gradient of vorticity and Δx_e is the element radius. The time integration is approximated by the trapezoid rule. Since the discrete velocity components u and v are linear functions in space and vorticity is a constant on each element, Ω_e, we therefore must approximate its spatial derivatives. To do this for an element Ω_e, the reconstruction scheme given in Appendix A.1 is applied using the constant element values of vorticity for the element Ω_e and those of its three edge element neighbors. The planar function from the reconstruction step with the maximum magnitude gradient is chosen and the derivatives of that function are used as approximations to the spatial derivatives of vorticity. For all element edges that lie on a physical boundary option two of the reconstruction scheme applies with the C_i value specified equal to zero (see Appendix A.1). Given the cumbersome nature of computing a vorticity gradient, we are able to justify vorticity, V, as a more efficient and practical visual indicator of high mass error based on the flow dynamics.

So it is proposed that vorticity, V, in combination with the geometric parameter, R_{max}, may provide further insight into the occurrence of mass error within these GWCE-based barotropic model applications. Such indicators may be useful in developing a systematic means of evaluating whether or not a GWCE-based model is appropriate for particular types of coastal dynamics applications. Furthermore, the indicators R_{max} and $\|D(v)_e\|$ may be applied as criteria for an adaptive meshing strategy or in the application of selective slope limiting when using a DG-based model for example. The two quantities, R_{max} and V, are now analyzed for several barotropic circulation problems that represent examples of wave-generated rip currents, wind-driven flows, and non-linear tidal dynamics to determine their suitability as indicators of mass imbalance in solutions computed using a GWCE-based circulation model.

3.2. Wave and wind—driven circulation

Two scenarios in which the driving force for coastal circulation is a surface stress are now considered. The first test problem describes a barred, sloping beach that has a channel cut through the bar (Fig. 3a). This bathymetric configuration is typically associated with the generation of offshore directed rip currents in the channel due to wave breaking along the bar. The beach is 750 m cross-shore (x-direction) by 1500 m alongshore (y-direction) with a bathymetric slope of 0.009. The bar, with a cross-shore width of 200 m, is located nearly 350 m offshore. A single channel, with a maximum alongshore width of 255 m, divides the bar at a position that is 7.5 m below the centerline of the domain. Note the asymmetry in this rip channel location. The finite element mesh for this domain resolves the bathymetry at 7.5 m using a uniform distribution of 20 301 nodes and 40 000 elements. The basin is closed by maintaining no-flow boundary conditions; the dimensions of the beach are selected to minimize lateral boundary interaction and allow realistic seaward flow of the rip current. The surface wave stress is computed as a radiation stress gradient derived from a wave height field generated by normally incident waves
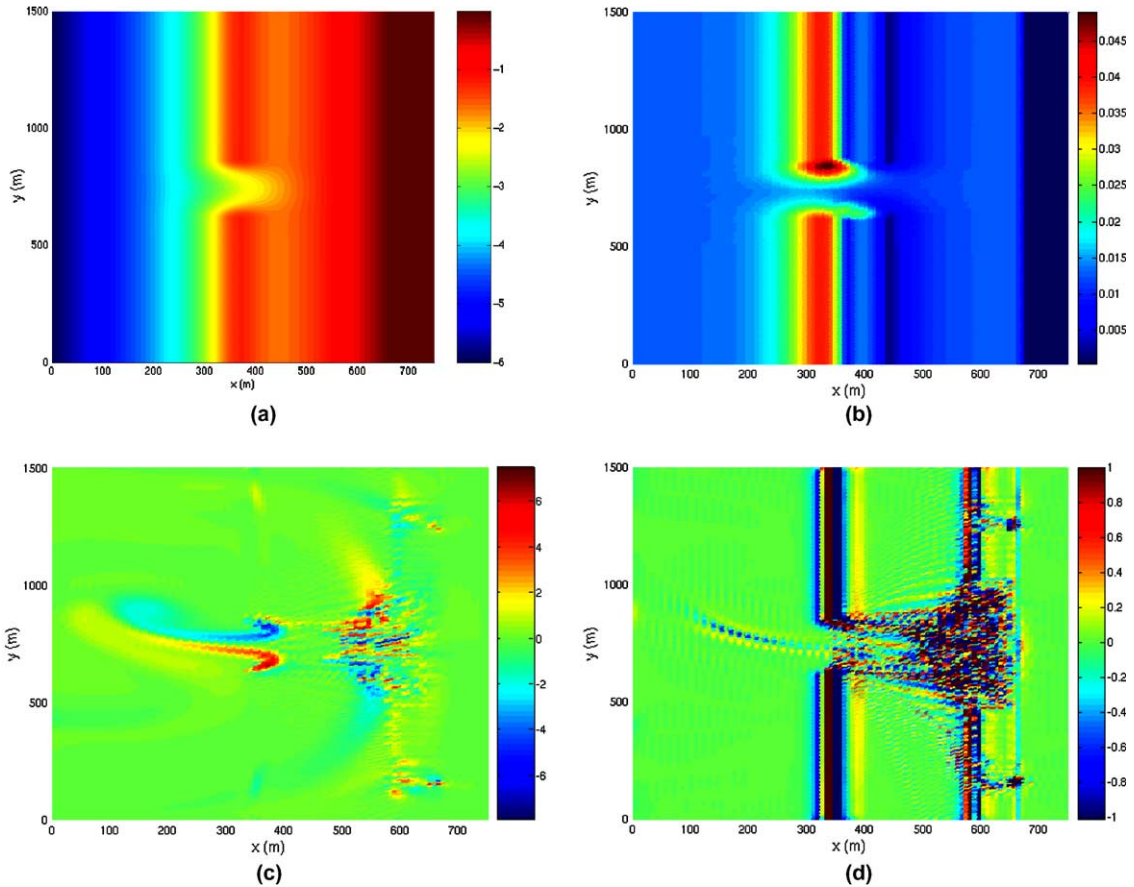
Fig. 3. For the barred beach with a rip channel, upon reaching steady-state after 14.4 h of simulation: (a) bathymetry (m), (b) R_{max}, (c) V, time-integrated vorticity of the currents, and (d) E_{mv}, mass error/volume (scales adjusted to bring out details).

of 10 s periods and initial height of 1.0 m. (See Cobb and Blain (2003) for details on generation of the surface wave field.) A time step of 0.0625 s is used and the lateral eddy viscosity is set to 1.0 m²/s. The GWCE weighting parameter, G, is specified as 0.01. Steady-state circulation is obtained after a simulation of 14.4 h and is described in detail by Cobb and Blain (2003). Since the mesh is uniform, differences in the value R_{max}, shown in Fig. 3b, are due to bathymetry gradients. Notice that the largest values of R_{max} occur in the region of the bar and that R_{max} is zero near the shore.

The computed vorticity, V, integrated in time over the 75 s interval leading up to hour 14.4, (Fig. 3c) reflects the position of the offshore directed rip current and the location of secondary breaking shoreward of the bar. In this shoreward region, circulation eddies constitute the return flow for the rip current and are a response to complex alongshore and cross-shore pressure gradients. Comparing the vorticity to the distribution of the mass error, E_{mv}, (Fig. 3d), a
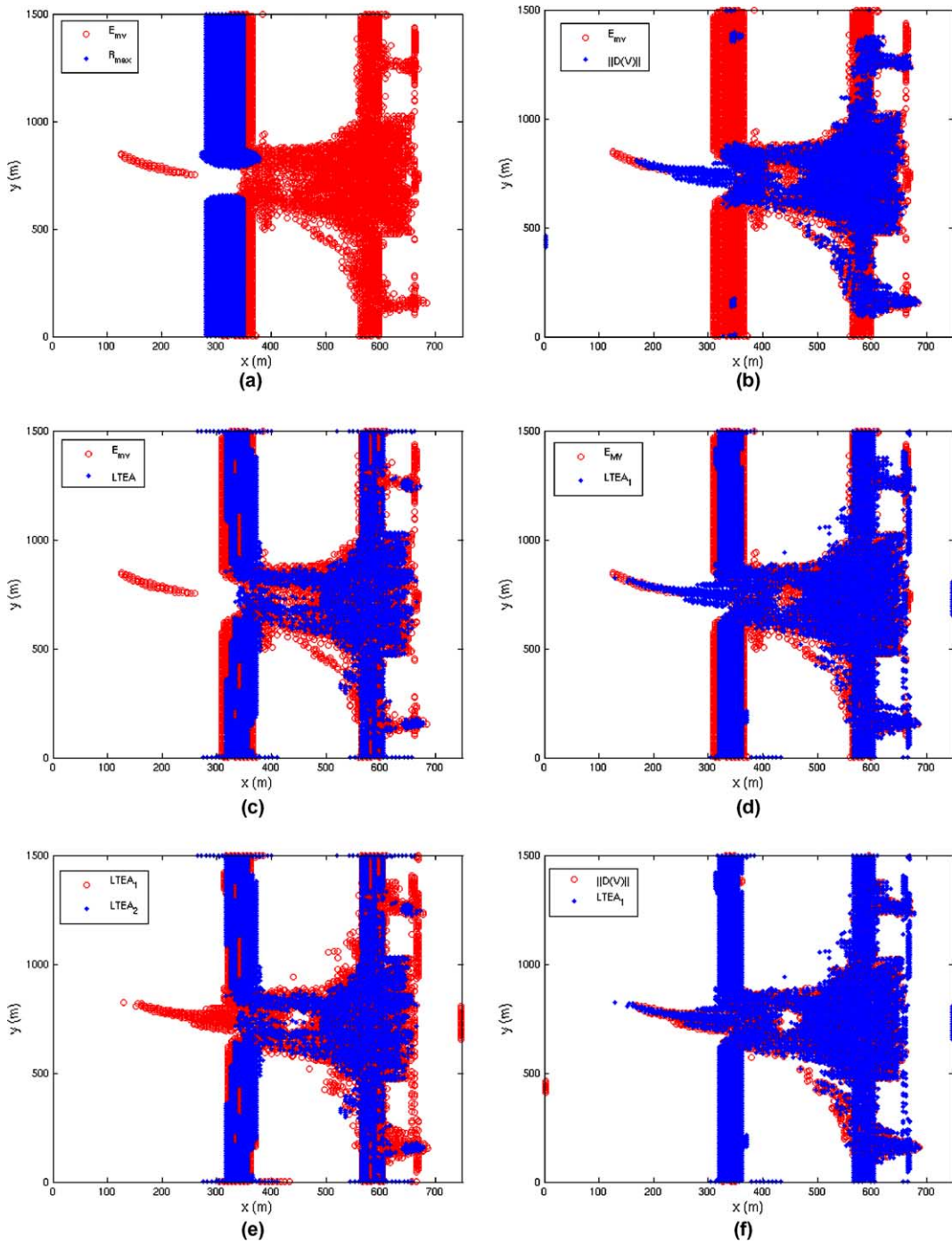
Fig. 4. For the barred beach with a rip channel, comparison of locations of statistically significant computed values for (a) E_{mv} versus R_{max}, (b) E_{mv} versus $\|D(V)_e\|$, (c) E_{mv} versus LTEA, (d) E_{mv} versus $LTEA_1$, (e) $LTEA_1$ versus $LTEA_2$, and (f) $\|D(V)_e\|$ versus $LTEA_1$.

correspondence between the magnitude of the mass error and spatial changes of vorticity, V, is seen in the region of secondary breaking and in the offshore flowing rip current. The strongest location of mass error is in the region of primary wave breaking on the bar as identified by higher R_{max} values over the bar; together spatial changes of vorticity, V, and R_{max} identify the regions of notable mass error associated with the rip current circulation. To quantify what is observed visually, Fig. 4 presents a series of overlays showing the locations of non-dimensional statistically significant values of the mass error, E_{mv}, versus R_{max}, the vorticity gradient, $\|D(V)_e\|$, LTEA, and LTEA$_1$. Overlays of LTEA$_1$ versus LTEA$_2$ and $\|D(V)_e\|$ versus LTEA$_1$ are also included. By statistically significant we mean the extreme values, ones located away from the mean value taken over the entire mesh. Specifically in the applications of Section 3.2 (rip current and rotating gyres) for E_{mv}, $\|D(V)_e\|$, LTEA, LTEA$_1$ and LTEA$_2$, we find all elements that have values that are more than 0.5 standard deviations above or below the respective mean value; for R_{max} all elements that have values more than 1.5 standard deviations above the mean value are labeled statistically significant. In the tidal application of Section 3.3, the upper and lower 5% of the extrema are labeled as statistically significant for all quantities considered; this criterion better represents the extreme values for a compressed range of very small mass error values. In Fig. 4a, the statistically significant values of R_{max} are confined to a region surrounding the bathymetric bar and extend the length of the bar in the alongshore direction. These locations nearly encompass all of the statistically significant mass error also occurring on and around the bar. Yet as is clear from Fig. 4a, R_{max} does not describe all the statistically significant mass error in the domain. By considering the locations of the statistically significant values of the vorticity gradient, shown in Fig. 4b, many of the high mass error locations not coincident with R_{max} are coincident with $\|D(V)_e\|$. The statistically significant values of the vorticity gradient, expressed as $\|D(V)_e\|$ are used here to quantify the spatial changes in vorticity that our eyes naturally detect in the visual interpretation of the vorticity field (Fig. 3c). The majority of the locations of extreme $\|D(V)_e\|$ shown in Fig. 4b are in the same region shoreward of the bar where secondary wave breaking is occurring with notable wave refraction and diffraction. The remaining locations of large vorticity gradients trace the offshore flowing rip current. In comparing the representation of extreme mass error locations by the indices R_{max} and $\|D(V)_e\|$, they clearly separate the occurrence of mass error by geometric properties, i.e. bathymetry gradients, and flow dynamics, respectively. Further analyses showing the locations of extreme mass error versus the locations of statistically significant values of LTEA and LTEA$_1$, Fig. 4c and d, respectively, demonstrate a close correspondence between the LTEA$_1$ and the occurrence of extreme vorticity gradients, $\|D(V)_e\|$ shown in Fig. 4b. The exception is the large values of LTEA$_1$ located on the bar. Of course these locations have already been identified by the index, R_{max}. Notice that although the entire LTEA captures many of the same locations of mass error along the bar and in the shoreward wave breaking region, the offshore directed rip current is not represented. Recall that the LTEA is composed of two local truncation error terms (Eq. (A.3.1)); the first term is primarily constructed of velocity gradients while the second term involves essentially only elevation gradients. The different locations that each of these two terms of the LTEA identify are shown in Fig. 4e. The major difference between the two terms is that the second term (LTEA$_2$) does not identify the location of the offshore directed rip current and captures fewer locations in the region of secondary breaking. Lastly by comparing the locations of statistically significant values of the vorticity gradient and the first term of the LTEA, i.e. LTEA$_1$ in Fig. 4f, excepting locations on the bar in which truncation error is caused the steep change in bathymetry,

the extreme values of the LTEA_1 and $\|D(V)_\text{e}\|$ are coincident. Together the results in Fig. 4d and f lend strong support to the validity of vorticity and in particular its gradients as an indicator of mass error. From the presented analyses, the quantity V, is presented as a theoretically based visual indicator of extreme mass error locations. The primary advantage of the vorticity, V, over its gradients $\|D(V)_\text{e}\|$ is that the computation of higher derivative terms are not required. Truly the combination of both $R_{\max}$ and V capture all locations of statistically significant mass error as is shown in Fig. 4a and b.

A second wind-driven problem is investigated in order to further examine the integrity of $R_{\max}$ and V as indicators of extreme mass error locations. Consider now a closed basin within which two closed gyres of rotating winds are propagated in a crossing pattern over a plane sloping bathymetry. The rectangular basin of dimension 450 m by 600 m is discretized using a structured triangular mesh containing 3691 nodes and 7200 elements. Elements are obtained by first dividing the basin into rectangles 15 m by 10 m and then creating four triangles per rectangle using the diagonals of the rectangle with the result being a maximum and minimum resolution of 8.125 m and 5.416 m, respectively. The bathymetry slopes linearly from an offshore maximum of 3.604 m to 0.01 m at the shoreline. The time step is set to 0.25 s, a lateral eddy viscosity coefficient is specified equal to $1.0 \, \text{m}^2/\text{s}$ and the GWCE weighting parameter has a value of 0.01. Zero elevation at the offshore boundary enforces a closed basin. Each rotating surface stress wind gyre varies linearly with the radius of the gyre; magnitude of the surface stress is zero at the center and reaches a maximum of $10 \, \text{N/m}^2$ at a distance of 50 m from the center. The simulation is for 14.4 h with a ramp of 12 h. The center of each gyre (100 m, 150 m) and (100 m, 450 m) is fixed in space for 13.2 h after which they begin to move linearly at an approximate speed of 0.0787 m/s. Both wind gyres rotate counter-clockwise and move in directions that are diagonally opposite such that they cross at (250 m, 300 m) near the center of the domain, with the resulting wind speeds being the vector sum of each gyre. The distribution of $R_{\max}$ is constant due to the plane sloping bathymetry and the uniform mesh spacing. Since the geometry of this problem does not pose any particular computational challenges, $R_{\max}$ is not expected to be a good indicator of mass error in the computed solution. Rather the vorticity of the flow field should serve as an appropriate mass error indicator. The vorticity of the circulation at 13.7 h, prior to the intersection of the rotating gyres, and the corresponding computed mass error are shown in Fig. 5a and b, respectively. Higher mass errors are located at the perimeter of the circulation gyres with the highest mass error values located at points where the vorticity gradient is most pronounced. This would correspond conceptually to regions of high velocity shear and advection which are thought to be a primary source of mass error in GWCE-based shallow water models. Similar to the rip current application examined previously, the statistically significant values of the mass error are overlaid by statistically significant values of the vorticity gradient, $\|D(V)_\text{e}\|$, LTEA, and LTEA_1 in Fig. 5c–e. Nearly all occurrences of extreme mass error are captured by the locations of statistically significant values of $\|D(V)_\text{e}\|$ in Fig. 5c. Comparing the correspondence between the LTEA and LTEA_1 with the locations of extreme mass error (Fig. 5d and e), values of LTEA_1 appear to represent more of the locations identified by E_{mv} than values for the entire LTEA. The correlation between $\|D(V)_\text{e}\|$ and LTEA_1 is reinforced by the coincident overlay of locations in Fig. 5f. For this wind-driven problem, the vorticity of the flow field and its gradients best represent the locations of extreme mass error in the computed solution.
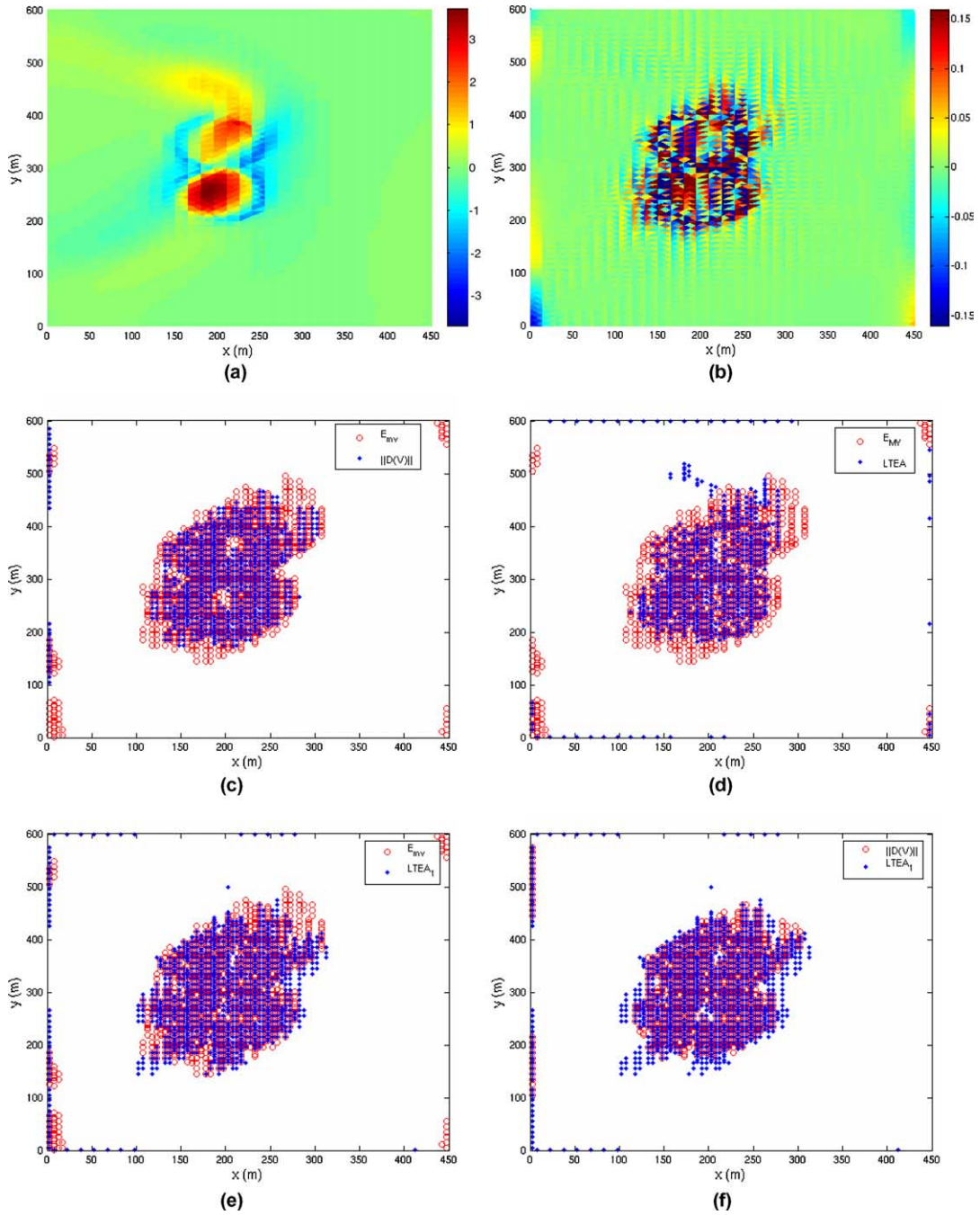
Fig. 5. For the wind-driven basin, 13.7 h into the simulation, computed (a) V, time-integrated vorticity, (b) E_{mv} mass error/volume, along with locations of statistically significant values of (c) E_{mv} versus $\|D(V)_e\|$, (d) E_{mv} versus LTEA, (e) E_{mv} versus LTEA$_1$, and (f) $\|D(V)_e\|$ versus LTEA$_1$.
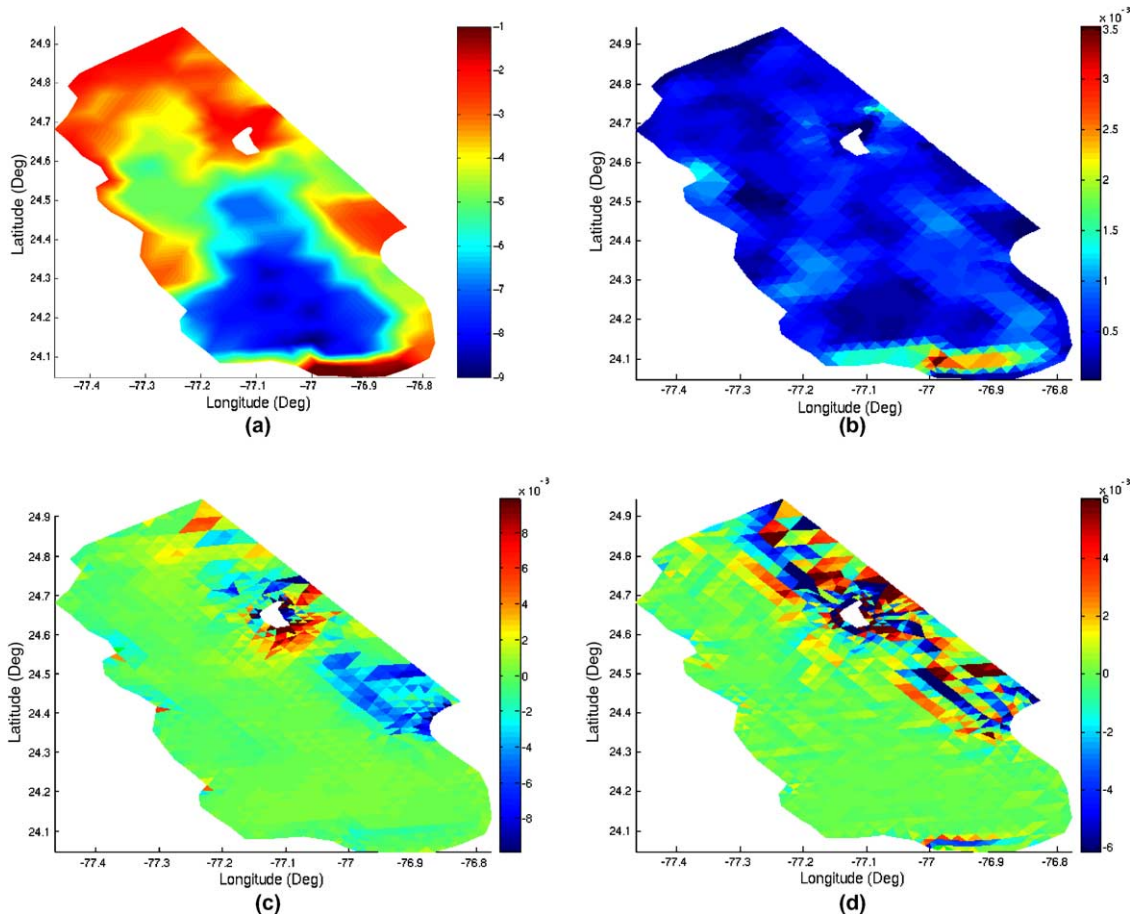
Fig. 6. For the Bight of Abaco: (a) bathymetry, (b) R_{max}, mean maximum bathymetric difference per element radius, (c) V, time-integrated vorticity of the currents (adjusted scales), and (d) E_{mv}, mass error/volume (adjusted scales).

3.3. Tidal dynamics

Lastly we consider a realistic tidal dynamics problem having variable bathymetry for which unstructured triangular meshes are applied. The application is a model of the tidal circulation in the Bight of Abaco, Bahamas, which lies between the islands of Great Abaco to the east, Little Abaco to the north, and Grand Bahama to the west. The basin, roughly 40 km by 100 km, is defined by a finite element mesh comprised of 1696 elements and 926 nodes resulting in a maximum and minimum resolution of 1750 m and 454 m, respectively. The time step is specified as 30 s, the GWCE weighting parameter, G, is set to 0.01, and lateral mixing effects are not considered. The tidal simulation undertaken extends for 12 days including a 5-day ramp period. Tidal forcing applied at the open ocean boundary and used to drive the simulation consists of five primary constituents (K_1, O_1, M_2, S_2, and N_2). The bathymetry varies from 1.0 m to 9.0 m (Fig. 6a). The Bight of Abaco is a site of significant non-linear tidal generation due to its isolation from deep offshore waters (1000–2000 m) and its own very shallow depths. Tides propagate from open waters and are
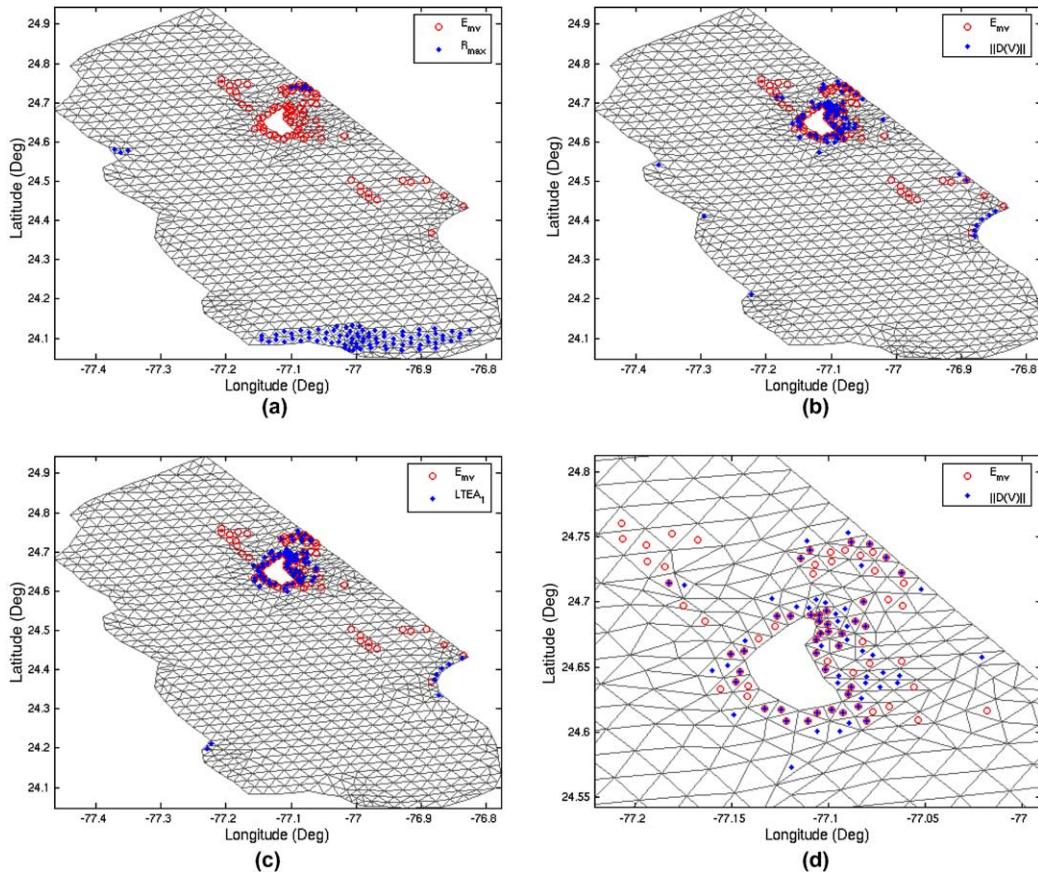
Fig. 7. For the Bight of Abaco: Comparisons of locations of statistically significant values of (a) E_{mv} versus R_{max}, (b) E_{mv} versus $\|D(V)_e\|$, (c) E_{mv} versus LTEA$_1$, and (d) E_{mv} versus $\|D(V)_e\|$ around the island.

largely modified by frictional dissipation and non-linear tidal interactions within the Bight. The Bight of Abaco has been extensively observed (Filloux and Snyder, 1979) and modeled (Westerink et al., 1989; Grenier et al., 1995) making it a well-suited field test case. This test problem is, however, typically well-represented using a GWCE-based model so mass errors overall are several orders of magnitude smaller than those computed for the two previous test problems.

For the Bight of Abaco application, the spatial variation in the parameter R_{max} is depicted in Fig. 6b. Larger values are found primarily at the transitions from very shallow depths to deeper ones around the perimeter of the basin and at transitions between the shallow sill at the entrance to the Bight and the deeper basin of the Bight. The computed vorticity and corresponding mass error after 11.6354 days of simulation are shown in Fig. 6c and d, respectively. In comparison to the distribution of mass error, both R_{max} and V identify regions of relatively larger mass error as identified in Fig. 6d. Mass error locations captured by significant values of R_{max}, shown in Fig. 7a, are located in the shallowest water near the open ocean boundary. The remaining significant R_{max} values shown are positioned at the shelf-slope transition in the southern Bight and identify the steepest bathymetry gradient with respect to the resolution of the mesh. The relation between

locations of statistically significant mass error and statistically significant vorticity gradients are shown in Fig. 7b. As has been shown in the prior applications, many of the locations of relatively significant mass error correspond to locations of significant vorticity gradients. These same locations are also indicative of statistically significant values of the $LTEA_1$ (Fig. 7c). Upon examination of an enlarged view surrounding the island presented in Fig. 7d, the overall correspondence between $\|D(V)_e\|$ and mass error is somewhat weaker than has been seen in the previous applications. A major difference for this particular application is the overall low (i.e. 10^{-3}) values of the mass error occurring throughout the domain (Fig. 6d). Though distributions of R_{max} and V shown in Figs. 6 and 7 are less dramatic in predicting locations of mass error than the previous flow cases, this is a direct result of the insignificant occurrence of mass error for this application. These low mass error values are not surprising since the tidal dynamics for this application are well-represented by GWCE-based models.

To summarize, while the parameter R_{max} may indicate fixed regions of mass loss for realistic applications it is not sufficient to identify all locations of mass error, whereby we see that the vorticity of the flow field is also revealing. The spatial variation of vorticity is demonstrated as a reliable indicator of high mass error regions in GWCE-based model solutions for tide and surface stress-driven coastal dynamics. This may not be surprising considering that vorticity is defined in terms of velocity gradients and it is advection dominated flows that are particularly problematic for GWCE-based shallow water models. As an indicator of mass error, the vorticity field may become a useful criterion in defining the need for a DG-based model and in the context of DG models, may indicate the locations for selective slope limiting.

4. Comparisons of GWCE and coupled DG–CG modeled solutions

Comparisons are made between solutions computed using the GWCE-based shallow water model ADCIRC and DG-ADCIRC, the model formulated using a coupled DG–CG approach. Water elevations within the DG-ADCIRC model are computed at the element center and denoted "DG". A node-based elevation is determined through an averaging procedure using elevation values at the neighboring elements and is labeled "DG-Avg". This nodally-averaged elevation is required for solution of the CG momentum equation; consequently, currents obtained from the momentum equation in DG-ADCIRC are nodal quantities, a consequence of the coupled DG–CG approach. For the DG–CG model solutions, mass is exactly conserved in the computation of elevation as expected from solution of the primitive continuity equation; mass imbalance computed using the conservative elevations is on the order of machine precision for all test problems. Some non-zero mass error is reintroduced into the momentum equation of the coupled DG–CG model through the averaging procedure by which elemental elevation values are assigned at nodal points (DG-Avg). This approach follows that of Dawson et al. (2004). In the future, more elegant approaches will be investigated that eliminate the reintroduction of mass error into the momentum equation.

Both the coupled DG–CG model and the GWCE-based model have been applied to several realistic and idealized test problems forced by winds, waves and tides. Presented here are two of the realistic test problems that represent extrema with respect to the influence of mass error on the computed solution. The two cases, Bight of Abaco, Bahamas and a barred beach with a

rip channel, are selected to demonstrate the capability of the coupled DG–CG model to produce robust solutions for both a traditional GWCE-based model application as well as a coastal dynamics problem described by highly advective, small scale flows.

4.1. Tidal dynamics—Bight of Abaco, Bahamas

Tidal dynamics within the Bight of Abaco (as described by the test problem in Section 3.3) are highly non-linear and their propagation is modified by the complex two dimensional variability of the region's bathymetry. Spatially solutions computed by the two models are seemingly identical (not shown) so to further investigate the impact of solving a DG primitive continuity equation, the elevation and velocity time series is examined at two elements, each selected from either a comparatively high or low mass error location. The differences between the two model solutions for elevation at the location of high mass error (element 1436) are shown in Fig. 8a. The CG–DG curve compares GWCE-computed elevations to elevations computed by the DG primitive continuity equation; CG–DG Avg indicates that differences are between GWCE-computed elevations and DG elevations averaged to the nodes. As discussed previously, the nodally averaged DG elevations are used for solution of the momentum equation. Comparisons of the water level differences (CG–DG) is manifest as a steeper slope in the tidal oscillation following each flood and ebb peak in Fig. 8a. This feature results in a slight phase lead by the DG-computed elevations as compared to the GWCE-computed elevations. The sign of the difference magnitude at peak flood and ebb convey that the amplitude of the DG-computed elevation is less than that computed by the GWCE-based model. Maximum elevation differences are on the order of 5 cm. By comparison, the nodally-averaged DG elevations are quite similar to the GWCE-computed elevations in terms of both phase and amplitude; a slight reduction in amplitude results in magnitude differences on the order of 0.5 cm. Clearly, some advantages of using the DG primitive continuity equation are
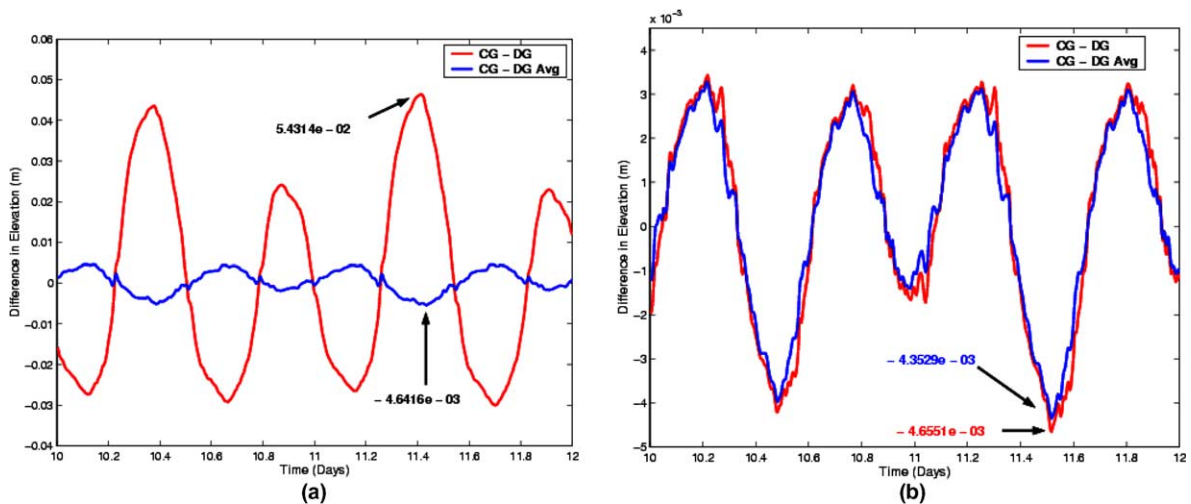

Fig. 8. For the Bight of Abaco, Bahamas, difference comparisons between elevations computed by the GWCE-based and coupled DG–CG models (m) at elements of comparatively (a) high mass error and (b) low mass error.
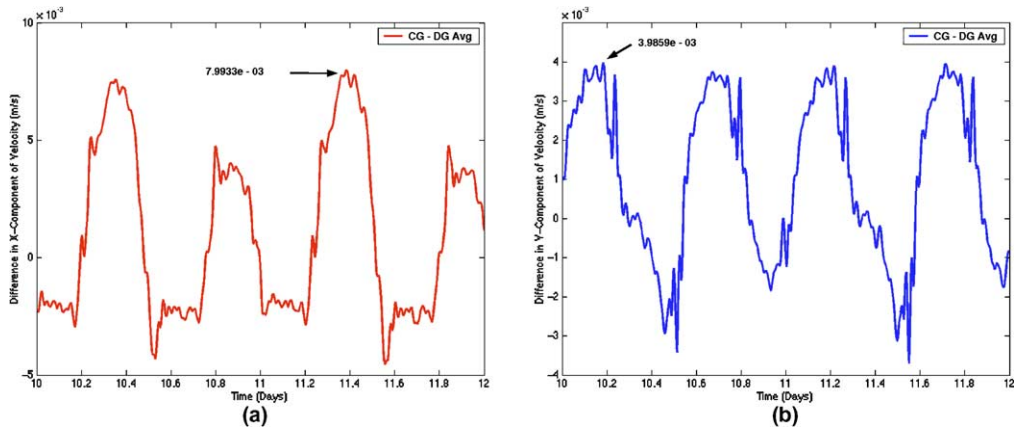
Fig. 9. For the Bight of Abaco, Bahamas, difference comparisons between the (a) *u*-component (m/s) and (b) *v*-component (m/s) of the current computed by the GWCE-based and coupled DG–CG models at an element of comparatively high mass error.

lost when converting to the nodal elevation values required for the CG momentum equation in the coupled DG–CG model. For this same high mass error element, the differences for each *u*- and *v*-component of the velocity field are small in comparing both models (Fig. 9a and b); differences for the primary flow direction (*u*) are no more than 0.8 cm/s and 0.1 cm/s differences are typical for the remaining flow direction (*v*). A cyclical pattern in the velocity differences is evident with negative differences in the *u*-component indicating that the coupled CG–DG model currents are greater than the GWCE-based currents particularly at peak ebb. Differences between the *v*-component velocities are more symmetric; positive values reveal that the coupled DG–CG model currents are slightly less in magnitude than the GWCE-based model currents. All differences in the current components are of comparable magnitude to the CG–DG Avg differences reported for elevation.

In contrasting elevation solutions at the high mass error element with those at an element of low mass error (element 335), as shown in Fig. 8b, one finds differences between the DG versus DG-Avg elevations far less significant when compared to GWCE-computed elevations; furthermore maximum elevations differences for either DG-based solution are no greater than 0.5 cm. Differences between the GWCE and coupled DG–CG solutions are less than 0.5 cm in elevation (Fig. 8b) and 0.1 cm/s in velocity (Fig. 10). In the primary flow direction (*u*-component, Fig. 10a), the differences are very small, i.e. hundredths of a cm, and oscillate at frequencies that are approximately 1/5 of dominant semi-diurnal tidal cycle.

To summarize, we observe that the coupled DG–CG solutions for this tidal flow problem are nearly identical to the GWCE-based solutions at locations where mass imbalance is comparatively small. At a location of comparatively high mass error, differences between the two model solutions are manifest primarily in the computed elevations, leading to phase differences on the order of 30–40 min and a nearly 20% reduction in the amplitude at peak flood and ebb. Adjustments of the ebb flow in the primary flow direction also result from the coupled DG–CG model. The behavior described is exactly what is desired of the new algorithm, to preserve the typically robust GWCE-based solutions where mass imbalance is not an issue and improve the solution in loca-
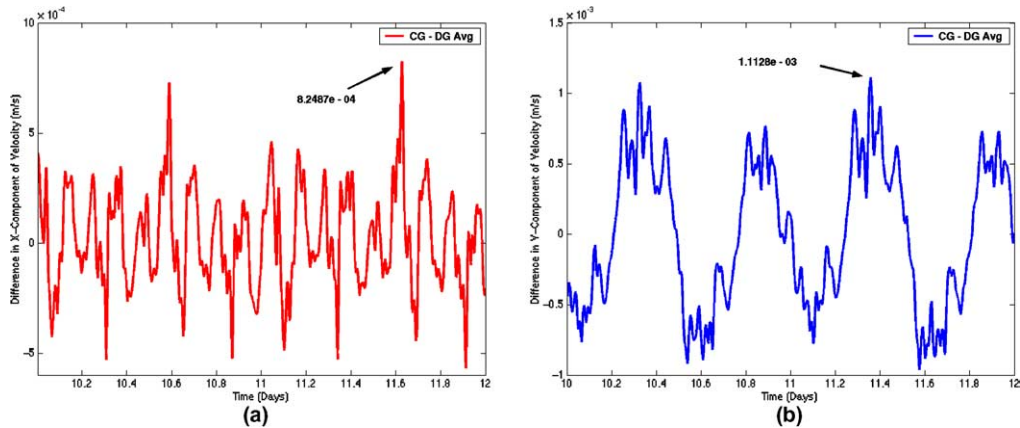
Fig. 10. For the Bight of Abaco, Bahamas, difference comparisons between the (a) *u*-component (m/s) and (b) *v*-component (m/s) of the current computed by the GWCE-based and coupled DG–CG models at an element of comparatively low mass error.

tions where mass error may lead to erroneous solutions. The differences reported here for the elevation and velocity fields are consistent with the magnitudes and types of error consistently reported for GWCE-based tidal solutions, (e.g. Edwards and Blain, 2001; Blain and Rogers, 1998). Furthermore, despite the reintroduction of some mass error via the nodally-averaged elevations (required for the continuous Galerkin momentum equation in the coupled DG–CG model), the effect of a conservative elevation solution is still evident in the magnitude of peak ebb currents in the primary flow direction for the Bight of Abaco. This result indicates potential benefits in using a coupled DG–CG method.

4.2. Wave-driven currents—barred beach with rip channel

The second realistic example presented is that of the barred sloping beach containing a rip channel discussed in Section 3.2. The coastal circulation typical of this scenario is described by small-scale (on the order of meters), highly advective flow processes. The anticipation is that the coupled DG–CG model will result in solutions that differ more significantly from those based on GWCE-type models which are known to produce errors for such problems. Water levels computed over the barred beach by the GWCE-based ADCIRC and the coupled DG–CG model are shown in Fig. 11a and b, respectively. Conceptually the two model solutions are quite similar, waves break first on the bar ($x = 350$ m) and then later in the rip channel ($x > 350$ m, $y = 750$ m) creating locations of set-down in elevation; the complex pattern in elevation nearest the shoreline ($x \sim 600$ m) is the signature of wave refraction and diffraction in the rip channel. Offshore, elevation set-down approaching the bar and a region of depressed elevation associated with the position of the rip current are evident in both model solutions. Though the general features of the two elevation solutions are similar, the differences in their detail are rather striking. Generally, the elevation features and, in particular, the elevation gradients are much sharper for the coupled DG–CG model solution. This is a direct consequence of the capability of the DG formulation to capture sharp discontinuities.
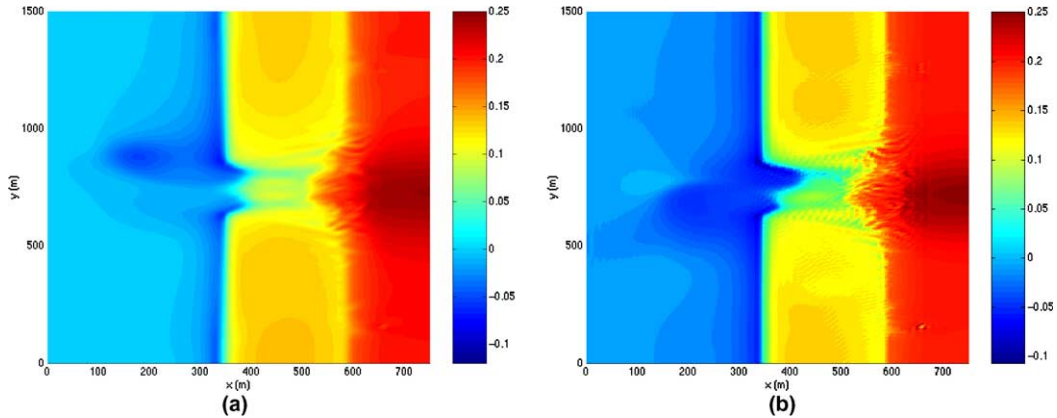
Fig. 11. For the barred beach with a rip channel, steady-state water levels (m) computed by the (a) GWCE-based and (b) coupled DG–CG models.

The corresponding steady-state circulation computed by the GWCE-based and coupled DG–CG models is shown in Fig. 12a and b, respectively. As was for elevation, the current pattern is conceptually similar but the details are quite different with respect to the position of the rip current and the asymmetries in the feeder current and alongshore currents between the bar (350 m) and the shoreline (750 m). The change in magnitude of the currents along the bar for the GWCE-based solution (Fig. 12a) which is absent in the coupled DG–CG solution (Fig. 12b) is directly correlated to the high mass error computed along the bar (Fig. 3d). Nearshore circulation associated with rip current generation is largely driven by complex along-shore and cross-shore pressure gradients that are initiated by wave breaking as the wave steepens moving over shallower depths such as a bar. A bar with a channel cut leads to alongshore variations in the wave steepening and breaking. These resulting alongshore variations in the elevation field are the primary driving force for the rip current generation. Thus accurate portrayal of the water elevation gradi-
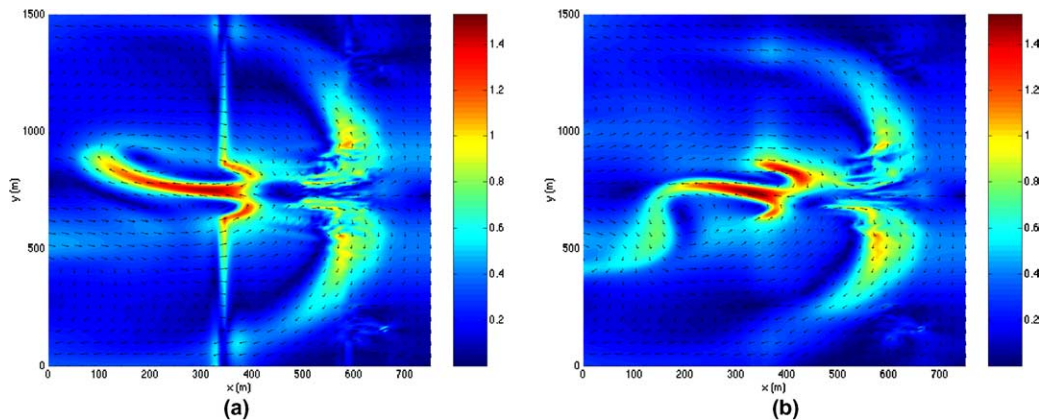

Fig. 12. For the barred beach with a rip channel, steady-state circulation (m/s) computed by the (a) GWCE-based and (b) coupled DG–CG models. Magnitude is shown in color; arrows indicate direction.

ents and the location of wave breaking are critical to capturing the rip current and its associated nearshore circulation. Nearshore circulation patterns and rip current generation in particular are the result of highly advective processes. Furthermore they are known to be quite sensitive to small changes in the bottom stress and/or lateral mixing, both very non-linear processes in this application. Consequently, differences between currents computed by the GWCE-based and coupled DG–CG models are not unexpected. One can surmise that the conservative elevation and sharp gradients computed by the coupled DG–CG model will likely lead to a more realistic representation of the steady-state nearshore circulation field. As such the coupled DG–CG model application to the barred beach with a rip channel indicates promise when considering replacement of a GWCE-based solution with that from the coupled DG–CG model.

5. Considerations for coupled DG–CG model applications

5.1. The application of slope limiters

The current slope limiter used in the coupled DG–CG model results in a somewhat heavy-handed limiter that tries to restrict local extrema of smooth solutions as well as spurious over-shoots and undershoots. This behavior is clearly shown by considering a channel that is 36 km long, 2 km wide and 10 m deep resolved to 250 m spacing. The open boundary is forced with an $8 \Delta x$ wave of amplitude 0.1 m. The computed elevation for the coupled DG–CG model with limiting is examined after 3267 s (Fig. 13a), a period which is long enough for 16 full waves to be in
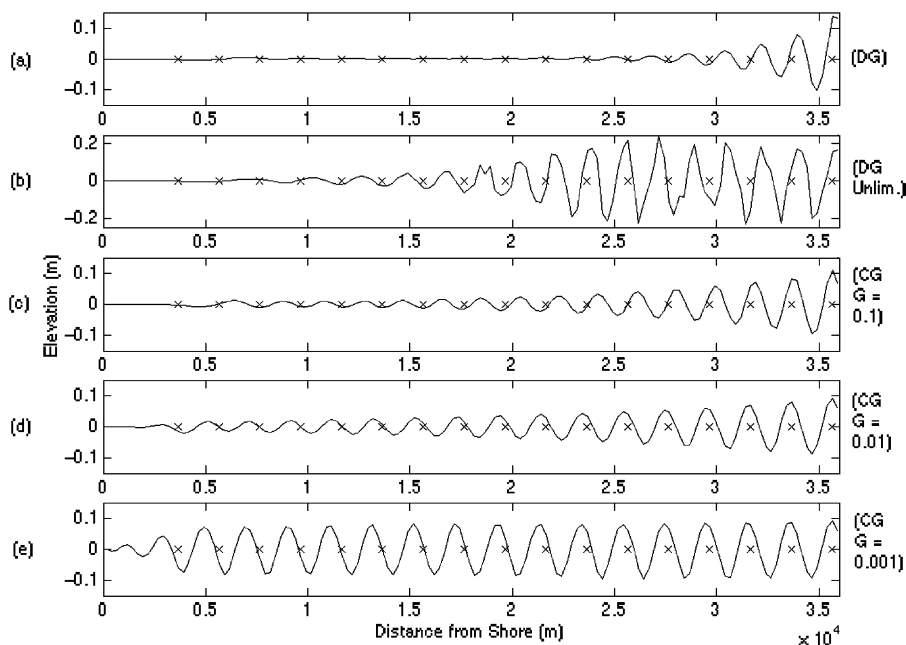

Fig. 13. For $8\Delta x$ waves in a channel, computed elevation solutions from the coupled DG–CG model (a) with slope limiting and (b) without slope limiting, and from the GWCE-based model for G values of (c) 0.1, (d) 0.01, and (e) 0.001.

the channel, yet none have reached the shoreline. Since this wave pattern is so short with respect to the grid resolution, the limiter will have a tendency to limit the crest and troughs in such a way as to decrease their amplitudes. Furthermore, this limiter aims to flatten out leading waves since the water elevation ahead of the wave is zero. The need for a slope limiter is clearly demonstrated by the nearly doubled elevation amplitudes in Fig. 13b that result from a coupled DG–CG solution in which slope limiters were not applied. Also included in Fig. 13 are three GWCE-based solutions with varying G values (Fig. 13c–e). Recall that the larger the value of G the more the GWCE approaches the primitive form of the continuity equation. One can view solution of the GWCE as a forced spring-oscillator with damping. The damping values correspond to the specification of G so that as G approaches zero, no damping is prescribed. The role of G is clearly demonstrated with the three GWCE-based solutions using G values of 0.1, 0.01, and 0.001 and presented in Fig. 13c–e, respectively. Note that although the unlimited DG solution (Fig. 13b) has larger predicted amplitudes its dissipation pattern is comparable to the GWCE-based solutions with high and moderate G values (Fig. 13c and d).

Further evidence that this coupled DG–CG method requires a slope limiter can be seen in Fig. 14 which depicts elevation solutions after 11.6354 days for the Bight of Abaco, Bahamas test problem. In Fig. 14a elevations are obtained from the coupled DG–CG solution using limiting and in Fig. 14b large oscillations in the elevation solution are occurring when slope limiting is not applied in the same model.

5.2. Computational cost for coupled DG–CG model applications

One of the major drawbacks to DG methods is that they require more degrees of freedom (DOF) because there are no continuity restrictions between elements. For two of the test problems considered, the total DOF required for solution of the elevation and velocities using the GWCE and coupled DG–CG formulations is compared in Table 1. Notice that the DOF for the GWCE model is $3N$ where N is the number of nodes (elevation and velocity), while the DOF for the coupled DG–CG model is computed as three times the number of elements (elevation) plus 2N (veloc-
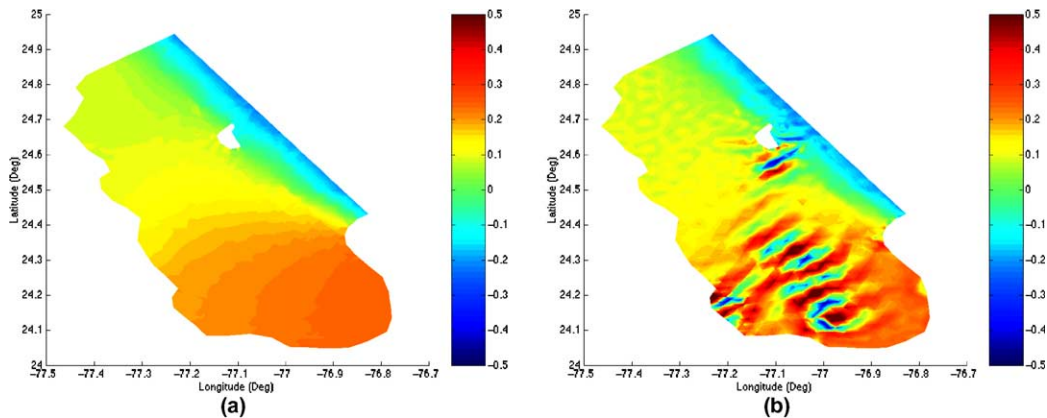

Fig. 14. For the Bight of Abaco, Bahamas, computed coupled DG–CG elevation solutions at 11.6354 days for (a) slope limiting active, and (b) no slope limiting.

Table 1
A comparison of the total degrees of freedom (DOF) required by the GWCE-based and coupled DG–CG solutions for the Bight of Abaco and the Rotating Gyres test problems

Test problem	No. elements	No. nodes	DOF GWCE	DOF DG–CG	DOF ratio
Bight of Abaco	1696	926	2778	6940	2.49
Rotating Gyres	7200	3691	11073	28982	2.62

Table 2
A comparison of computational times for the GWCE-based and coupled DG–CG solutions for the Bight of Abaco and the Rotating Gyres test problems

Test problem	No. time steps	GWCE (s)	DG–CG (s)	Ratio of CPU increase
Bight of Abaco	34560	142	391	2.75
Rotating Gyres	207360	3413	9728	2.85

ity). The DOF for the coupled DG–CG model can be approximated as 8N using a nodal connectivity estimate of 6 elements/node. The theoretical increase in the DOF for the coupled DG–CG model over the GWCE-based model is a factor of approximately 2.6.

Table 2 details the computational cost of these extra DOF by comparing single processor computational times for both the GWCE-based and coupled DG–CG elevation solutions for the two problems in Table 1. All computations are performed on a machine with dual 32 bit 2.4 GHz Intel Xeon processors with 4 GB of memory using Red Hat Linux 8.0 as the operating system; code compilation is achieved using Portland Group FORTRAN 90.

Though the coupled DG–CG model does have additional costs associated with the projection of the DG elevation solution back into a continuous (nodal) space in order to compute the CG components of the momentum equation, these costs are not significant. Rather the increase in DOF is the cause of the additional expense associated with the coupled DG–CG method as seen by comparing the DOF ratio in Table 1 with the ratio of CPU increase in Table 2. To summarize, when compared to the GWCE-based formulation of ADCIRC, the coupled DG–CG code requires roughly three times more computational time per time step.

Though the lack of continuity required by the coupled DG–CG formulation increases the DOF, it is also what makes it a local method, meaning that intra-element interactions occur only between an element and its immediate edge neighbors through the flux terms, i.e. each element communicates with only three element neighbors, whereas in the CG formulation, each element communicates with on average 12 other elements. This compact communication structure for the DG method gives rise to the possibility of very efficient and simple parallelization strategies. Furthermore, as Flaherty et al. (2002) suggest, when a DG code is written for efficient parallelization, the extra computational time due to the additional degrees of freedom may be overcome by the efficiency of the parallelization. Thus large scale problems may still realistically be solved. Additionally, when compared with the GWCE-based formulation, the DG method can easily achieve a higher order of accuracy, without increasing the intra-element communication pattern. This allows a potential decrease in the number of elements and thereby a reduction in the computational cost while maintaining the same overall order of accuracy as a GWCE-based model.

6. Concluding remarks

Mass imbalances present in the water levels and circulation computed by GWCE-based continuous Galerkin finite element coastal ocean models have been meticulously documented herein for representative coastal applications driven by tide, wind and wave dynamics. The locations of statistically significant mass error exhibit a direct correspondence to either the vorticity gradients of the circulation or the ratio of the mean maximum bathymetric difference to the element radius for nearly all dynamical cases considered. Locations of statistically significant extrema of the vorticity gradients are shown to be coincident with the first term of the local truncation error (LTEA$_1$) for the momentum equation in GWCE-based models. Both the LTEA$_1$ and the vorticity gradients are coincident with high mass error locations. A robust indicator of mass error such as the vorticity as observed here can be used to assess the necessity for a locally conservative scheme in the computational algorithm or validate the application of a GWCE-based model. Such indicators may also be used in the future with so called flexible Galerkin algorithms for which some level of continuity in space can be maintained (Massey, 2002).

Despite the existence of mass error, many tide and wind-driven applications simulated using GWCE-based models are quite robust and yield excellent solutions of the coastal ocean state under barotropic conditions. As shown herein, as advection and small scale processes become more important to the overall circulation, such as for the rip current generation, mass errors can become significant within GWCE-based calculations with the result being a solution that deviates notably from that derived using a conservative coupled DG–CG method.

The need to move towards a locally conservative formulation for finite-element based coastal models is clear. DG methods are locally conservative by their definition and higher-order DG methods offer even more accuracy and flexibility than more common FV methods. In comparing the GWCE-based and coupled DG–CG model solutions for the dynamically extreme cases of tide and wave-driven scenarios, the coupled DG–CG formulation is able to retain the robustness of the GWCE-based solutions for the typical tide-driven application explored here while at the same time computing sharper gradients in the solution of elevation and currents. Resolution of these small-scale features have a notable effect on the highly advective non-linear flow fields associated with nearshore flows such as the generation of a rip current on a barred beach examined within.

Of course, no method is perfect and there are several considerations associated with the application of coupled DG–CG methods that are being currently addressed. The need for a slope limiting procedure in DG-based models is understood but how the limiting procedure influences the final solution requires more investigation. Care must be taken in formulating a slope limiter that minimizes overshoots and undershoots but does not diminish smooth local extrema. This is an area of intense research. Lastly, DG methods with nearly three times the number of degrees of freedom associated with CG methods are comparatively three times more expensive in head-to-head serial comparisons. However, the local and highly parallelizable nature of the method is expected to overcome these extra computations. In addition, the higher order DG methods can use less resolved grids and achieve the same overall order of accuracy as CG methods with an additional reduction in the degrees of freedom, without complicating intra-element communication patterns. Certainly, the coupled DG–CG model eliminates the mass imbalance associated with current GWCE-based CG coastal ocean models and leads to robust realistic representations of coastal ocean dynamics suitable for use with transport models.

Appendix A

A.1. A simple linear reconstruction scheme

In order to approximate the spatial derivatives of an element averaged constant function C_e, we first consider an interior element Ω_e along with its edge neighboring elements, Ω_i, $i = 1, 2, 3$, as shown in Fig. A.1.1. We partially construct three interpolating planar functions, see Zwillinger (1996) for reference, using the element averaged constant values, $\{C_i\}$, $i = e, 1, 2, 3$ and the barycenter coordinates (x_i, y_i) of the elements given,

(1) Ω_1 Ω_e Ω_2,
(2) Ω_2 Ω_e Ω_3,
(3) Ω_3 Ω_e Ω_1,

and then find their gradients. For example, to find the spatial derivatives of the first planar function, C^1, passing through the points, (x_1, y_1, C_1), (x_e, y_e, C_e), and (x_2, y_2, C_2), we first take the cross product,

$$\begin{bmatrix} x_1 - x_e \\ y_1 - y_e \\ C_1 - C_e \end{bmatrix} \times \begin{bmatrix} x_1 - x_e \\ y_2 - y_e \\ C_2 - C_e \end{bmatrix} = \begin{bmatrix} i & j & k \\ (x_1 - x_e) & (y_1 - y_e) & (C_1 - C_e) \\ (x_1 - x_e) & (y_2 - y_e) & (C_2 - C_e) \end{bmatrix} \doteq d_1 \mathbf{i} + d_2 \mathbf{j} + d_3 \mathbf{k},$$
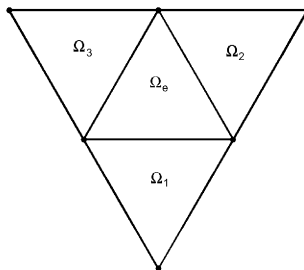
$$(A.1.1)$$

Fig. A.1.1. An interior element with its edge neighbors.

which is normal to the plane. Then the derivatives of the first planar function, C^1, are simply

$$\frac{dC^1}{dx} = -\frac{d_1}{d_3}, \quad \text{and} \quad \frac{dC^1}{dy} = -\frac{d_2}{d_3}.$$

Note that if one of the edges of Ω_e lies on a boundary then we can choose one of two options, first, we can reflect element Ω_e across that edge and use the resulting reflection as the neighbor element and value in the reconstruction step. The second option is to use a specified value for C_i and the midpoint of that edge in the reconstruction step.

A.2. A slope limiter

The current slope limiter implemented in the coupled DG–CG model is based on the reconstruction scheme outlined in Section A.1.1. Given an element Ω_e and its DG elevation solution from Eq. (7), we compute the approximate interpolated derivatives associated with this element and its edge neighbors using the reconstruction scheme. We then compare the magnitude of the gradient of all three interpolated functions with that of the DG elevation solution itself on element Ω_e. The slopes for the DG solution, from Eq. (7), on element Ω_e are then set based on the minimum magnitude gradient of all four possible planes. For edges that lie on a land boundary, option one in the reconstruction scheme is used for the neighbor value. If the edge is an open sea boundary, option two of the reconstruction scheme is used with the value of the specified elevation at the midpoint of that edge as the neighbor element average.

A.3. Local truncation error

Hagen et al. (2001) presented for GWCE-based models, an estimate to the leading term of the truncation error (LTEA) associated with the discrete form of the linear, harmonic, non-conservative momentum equations on the interior nodes of an equilateral triangular mesh. We present that error here without development. A harmonic form of the non-conservative momentum equation is determined by letting, $u = \hat{u}e^{\hat{i}wt}$, $v = \hat{v}e^{\hat{i}wt}$, and, $\zeta = \hat{\zeta}e^{\hat{i}wt}$ where, $\hat{u}$, $\hat{v}$, and $\hat{\zeta}$ are the complex amplitudes of u, v, and ζ, $\hat{i} = \sqrt{-1}$ and ω = the response frequency. The result, following Hagen et al. (2001) is an expression for the LTEA:

$$\begin{aligned}
\text{LTEA} = \Delta x_e^2 \left(\frac{\hat{i}\omega + \tau}{2} \right) \left(\frac{\partial^2 \hat{u}_k}{\partial x^2} + \frac{\partial^2 \hat{v}_k}{\partial x^2} + \frac{\partial^2 \hat{u}_k}{\partial y^2} + \frac{\partial^2 \hat{v}_k}{\partial y^2} \right) \\
+ \Delta x_e^2 \frac{g}{2} \left(\frac{\partial^3 \hat{\zeta}_k}{\partial x^3} + \frac{\partial^3 \hat{\zeta}_k}{\partial x^2 \partial y} + \frac{\partial^3 \hat{\zeta}_k}{\partial x \partial y^2} + \frac{\partial^3 \hat{\zeta}_k}{\partial y^3} \right) + O(\Delta x_e^4).
\end{aligned} \tag{A.3.1}$$

Each term in the LTEA can be written separately, namely the first terms,

$$\text{LTEA}_1 = \Delta x_e^2 \left(\frac{\hat{i}\omega + \tau}{2} \right) \left(\frac{\partial^2 \hat{u}_k}{\partial x^2} + \frac{\partial^2 \hat{v}_k}{\partial x^2} + \frac{\partial^2 \hat{u}_k}{\partial y^2} + \frac{\partial^2 \hat{v}_k}{\partial y^2} \right), \tag{A.3.2}$$

and the second terms,

$$\text{LTEA}_2 = \Delta x_e^2 \frac{g}{2} \left(\frac{\partial^3 \hat{\zeta}_k}{\partial x^3} + \frac{\partial^3 \hat{\zeta}_k}{\partial x^2 \partial y} + \frac{\partial^3 \hat{\zeta}_k}{\partial x \partial y^2} + \frac{\partial^3 \hat{\zeta}_k}{\partial y^3} \right). \tag{A.3.3}$$

These quantities are then made non-dimensional by an integration in time over all subintervals $[t_k, t_k + \Delta t]$ in the time interval $[t_0, t]$, then multiplication by Δt and division by Δx_e.

References

Alcrudo, F., Garcia-Navarro, P., 1993. A high-resolution Godunov-type scheme in finite volumes for the 2D shallow water equations. International Journal of Numerical Methods in Fluids 16, 489–505.

Aizinger, V., Dawson, C., 2002. Discontinuous Galerkin methods for two-dimensional flow and transport in shallow water. Advances in Water Resources 25, 67–84.

Blain, C.A., Cobb, M., 2003. Application of a shelf-scale model to wave-induced flow. Longshore Currents on Plane and Barred Beaches. NRL Formal Report, NRL/FR/7322-03-10,046, Naval Research Laboratory, Department of the Navy, March 11, 2003.

Blain, C.A., Rogers, W.E., 1998. Coastal tidal prediction using the ADCIRC-2DDI hydrodynamic finite element model. NRL Formal Report, NRL/FR/7322-98–9682, Naval Research Laboratory, Department of the Navy, December 18, 1998.

Blain, C.A., Westerink, J.J., Luettich Jr., R.A., 1998. Grid convergence studies for the prediction of hurricane storm surge. International Journal of Numerical Methods in Fluids 26, 369–401.

Blain, C.A., Westerink, J.J., Luettich Jr., R.A., 1994. The influence of domain size on the response characteristics of a hurricane storm surge model. Journal of Geophysical Research 99, 18467–18479.

Berger, R.C., Howington, S.E., 2001. Discrete fluxes and mass balance in finite elements. Journal of Hydraulic Engineering 128 (1), 87–92.

Buhler, O., Jacobson, T.E., 2001. Wave-driven currents and vortex dynamics on barred beaches. Journal of Fluid Mechanics 449, 313–339.

Cobb, M., Blain, C.A., 2003. Application of a shelf-scale model to wave-induced flow, Rip currents. NRL Formal Report, NRL/FR/7322-03-10,055, Naval Research Laboratory, Department of the Navy, 28 pp.

Chippada, S., Dawson, C.N., Martinez, M.L., Wheeler, M.F., 1998. A Godunov-type finite volume method for the system of shallow water equations. Computational Methods in Applied Mechanical Engineering 151, 105–129.

Cockburn, B., Hou, S., Shu, C.-W., 1990. The Runge–Kutta local projection discontinuous Galerkin finite element method for conservation laws IV: The multidimensional case. Mathematics of Computation 54 (190), 545–581.

Cockburn, B.G., Karniadakis, E., Shu, C.-W. (Eds.), 2000. Discontinuous Galerkin Methods: Theory, Computation and Application. Lecture Notes in Computational Science and Engineering, vol. 11. Springer, Berlin, 470 pp.

Cockburn, B., Shu, C.-W., 1998. The Runge–Kutta discontinuous Galerkin method for conservation laws V: Multidimensional systems. Journal of Computational Physics 141, 199–224.

Dawson, C., Proft, J., 2002. Discontinuous and coupled continuous/discontinuous Galerkin methods for the shallow water equations. Computer Methods in Applied Mechanics and Engineering 191, 4721–4746.

Dawson, C., Westerink, J.J., Pothina, D., Feyen, J., 2004. Continuous, discontinous and coupled discontinuous–continuous Galerkin finite element methods for the shallow water equations. International Journal of Numerical Methods in Fluids, submitted for publication.

Edwards, C.R., Blain, C.A., 2001. A Evaluation of tidal modeling strategy in the Yellow Sea: Large domains versus limited area models. NRL Formal Report, NRL/FR/7320-01-9976, Naval Research Laboratory, Department of the Navy, September 4, 2001.

Filloux, J.H., Snyder, R.L., 1979. A study of tides, setup and bottom friction in a shallow semi-enclosed basin. Part I: Field experiment and harmonic analysis. Journal of Physical Oceanography 9, 158–169.

Flaherty, J.E., Krivodonova, L., Remacle, J.F., Shephard, M.S., 2002. Aspects of discontinuous Galerkin methods for hyperbolic conservation laws. Finite Elements in Analysis and Design 38, 889–908.

Fortunato, A.B, Baptista, A.M., Luettich Jr., R.A., 1998. A three-dimensional model of tidal currents at the mouth of the Tagus Estuary. Continental Shelf Research 17 (14), 1689–1714.

Giraldo, F.X., Hesthaven, J.S., Warburton, T., 2002. Nodal high-order discontinuous Galerkin methods for the spherical shallow water equations. Journal of Computational Physics 181, 499–525.

Guillot, M.J., Blain, C.A., 2003. Implementation of a discontinuous Galerkin discretization of the conservation of mass equation in QUODDY, NRL Formal Report, NRL/FR/7322–03-10,050, Naval Research Laboratory, Department of the Navy, 18 pp.

Grenier, R.R., Luettich, R.A., Westerink, J.J., 1995. A Comparison of the nonlinear frictional characteristics of two-dimensional and three-dimensional models of a shallow tidal embayment. Journal of Geophysical Research 100 (C7), 13719–103735.

Hagen, S.C., Westerink, J.J., Kolar, R.L., 2000. One-dimensional finite element grids based on a localized truncation error analysis. International Journal of Numerical Methods in Fluids 32, 241–261.

Hagen, S.C., Westerink, J.J., Kolar, R.L., Horstmann, O., 2001. Two-dimensional unstructured mesh generation for tidal models. International Journal of Numerical Methods in Fluids 35, 669–686.

Hannah, C.G., Wright, D.G., 1995. Depth dependent analytical and numerical solution for wind-driven flow in the coastal ocean. In: Lynch, D.R., Davies, A.M. (Eds.), Quantitative Skill Assessment for Coastal Ocean Models, vol. 47, Coastal and Estuarine Studies. American Geophysical Union, Washington, DC, pp. 125–152.

Kinnmark, I., 1986. The Shallow Water Wave Equations: Formulation, Analysis, and Application. Lecture Notes in Engineering, vol. 15. Springer-Verlag, Berlin, 187 pp.

Kolar, R.L., Westerink, J.J., 2000. A look back at 20 years of GWCE-based shallow water models. In: Bentley, L.R. et al. (Eds.), Computational Methods in Water Resources XIII, 2, Surface Water Systems and Hydrology. A.A. Balkema, Rotterdam.

Kolar, R.L., Westerink, J.J., Cantekin, M.E., Blain, C.A., 1994. Aspects of nonlinear simulations using shallow water models based on the wave continuity equation. Computers and Fluids 23 (3), 523–538.

LeRoux, D., Staniforth, A., Lin, C.A., 1998. Finite elements for shallow-water ocean models. Monthly Weather Review 1931–1951, 126.

Luettich Jr., R.A., Hench, J.L., Fulcher, C.W., Werner, F.E., Blanton, B.O., Churchill, J.H., 1999. Barotropic tidal and wind-driven larval transport in the vicinity of a barrier island inlet. Fisheries Oceanography 8 (Suppl. 2), 190–209.

Luettich, R.A., Muccino, J.C., Foreman, M.G.G., 2002. Considerations in the calculation of vertical velocity in three-dimensional circulation models. Journal of Atmospheric and Oceanic Technology 19, 2063–2076.

Luettich, R.A., Westerink, J.J., 1995. Continental shelf-scale convergence studies with a barotropic tidal model. In: Lynch, D.R., Davies, A.M. (Eds.), Quantitative Skill Assessment for Coastal Ocean Models, vol. 47, Coastal and Estuarine Studies. American Geophysical Union, Washington, DC, pp. 349–371.

Luettich, R.A., Westerink, J.J., 2003. Formulation and numerical implementation of the 2D/3D ADCIRC finite element model version 43.XX, 7 February, 2003. Internal report, Available from <http://www.marine.unc.edu/C_CATS/adcirc/document/theory_report/adcirc_3D_02_07_03.pdf>.

Luettich, R.A., Westerink, J.J., Scheffner, N.W., 1992. ADCIRC: An advanced three-dimensional circulation model for shelves, coasts, and estuaries. Report 1: Theory and methodology of ADCIRC-2DDI and ADCIRC-3DL. Technical Report DRP-92-6, USAE, Vicksburg, MS, 137 pp.

Lynch, D.R., 1985. Mass balance in shallow water simulations. Communications in Applied Numerical Methods 1, 153–159.

Lynch, D.R., Gray, W.G., 1979. A wave equation model for finite element tidal computations. Computers and Fluids 7 (3), 207–228.

Lynch, D.R., Holboke, M.J., 1997. Normal flow boundary conditions in 3D circulation models. International Journal of Numerical Methods in Fluids 25, 1185–1205.

Lynch, D.R., Officer, C.B., 1985. Analytic test cases for three dimensional hydrodynamic models. International Journal of Numerical Methods in Fluids 5, 539–543.

Massey, T.C., 2002. A flexible Galerkin finite element method with an a posteriori discontinuous finite element error estimation for hyperbolic problems. Ph.D. thesis, Virginia Polytechnic Institute and State University, Department of Mathematics.

Massey, T.C., Blain, C.A., 2004. Consistent mass flux computation for a GWCE based shallow water model. Computational Methods in Applied Mechanical Engineering, submitted for publication.

Navon, I.M., 1988. A review of finite-element methods for solving the shallow-water equations. In: Schrefler, Zienkiewicz (Eds.), Computer Modelling in Ocean Engineering. pp. 273–278.

Oliveira, A., Fortunato, A.B., Baptista, A.M., 2000. Mass balance in Eulerian–Lagragian transport simulations in estuaries. Journal of Hydraulic Engineering 126 (8), 605–614.

Reed, W.H., Hill, T.R., 1973. Triangular mesh methods for the neutron transport equation, Tech. Report LA-UR-73-479, Los Alamos Scientific Laboratory.

Schwanenberg, D., Kongeter, J., 2000. Discontinuous Galerkin method for shallow water equations with source terms. In: Cockburn, B. (Ed.), Discontinuous Galerkin Methods: Theory, Computation, and Application, Lecture Notes in Computational Science and Engineering, vol. 11. Springer, Berlin, pp. 419–424.

Walters, R.A., 1983. Numerically induced oscillations in finite element approximations to the shallow water equations. International Journal for Numerical Methods in Fluids 3, 591–604.

Westerink, J.J., Gray, W.G., 1991. Progress in Surface Water Modeling. Reviews in Geophysics (Suppl.) 29, 210.

Westerink, J.J., Luettich, R.A., Muccino, J.C., 1994. Modeling tides in the western North Atlantic using unstructured graded grids. Tellus 46A, 178–199.

Westerink, J.J., Stolzenbach, K.D., Conner, J.J., 1989. General spectral computations of the nonlinear shallow water tidal interactions within the Bight of Abaco. Journal of Physical Oceanography 19 (9), 1348–1371.

Zhang, Y.L., Baptista, A.M., 2000. An efficient adaptive editor for Unstructured grids. Numerical Grid Generation in Computational Field Simulations, The International Society of Grid Generation, pp. 395–404.

Zwillinger, D. (Ed.), 1996. CRC Standard Mathematical Tables and Formulae, 30th ed. CRC Press, New York.